aerospace

MDPI

Article

Vibration Suppression and Bifurcation Analysis of a Two-DOF Structure Coupled with PMNES

Ming Yang [1], Jingjun Lou [1], Qingchao Yang [1,*], Jiawen Chu [1], Kai Chai [1], Maoting Tan [1], Juan Wang [1], Xu Bao [1] and Tao Lin [2]

[1] College of Naval Architecture and Ocean Engineering, Naval University of Engineering, Wuhan 430033, China; yangming1812@163.com (M.Y.)
[2] School of Civil Engineering, Chongqing University, Chongqing 400045, China
* Correspondence: 1405061065@nue.edu.cn

Abstract

Vibration is a critical issue in aerospace structures, where lightweight design, high flexibility, and complex operational environments often lead to pronounced nonlinear dynamic responses. Excessive vibrations induced by harmonic excitations, aerodynamic loads, or onboard equipment can significantly degrade structural integrity, control accuracy, and service life. Consequently, advanced passive vibration suppression techniques with strong robustness and broadband effectiveness are of great importance in aerospace engineering applications. The bifurcation boundary and vibration suppression performance of Piezoelectric–Monostable Nonlinear Energy Sink (PMNES) are crucial for evaluating its effectiveness on the main structure. To simplify the analysis of flexible aerospace structures, a reduced-order model is derived by modal truncation in the low-frequency range, which is then treated as a two-degree-of-freedom main structure. To focus on the underlying nonlinear dynamic mechanisms, an equivalent two-degree-of-freedom lumped-parameter system is adopted as a generic representation of the dominant low-frequency dynamics of flexible aerospace structures. In this work, the electromechanical coupling control equations of the system of a two-degree-of-freedom main structure coupled with PNES are derived through the application of Newton's second law and Kirchhoff's voltage law. The methods of complexification-averaging (CX-A) and Runge–Kutta (RK) are employed to assess the vibration suppression performance and stability characteristics of the system under harmonic excitation. The approximate solution is validated through numerical solutions. The approximate solutions of the system are employed to derive the Saddle Node (SN) bifurcation and codimension-two cusp bifurcation points, while the enhanced algorithm is employed to ascertain the most unfavorable amplitude at each external excitation circular frequency and to determine whether the mark represents a Hopf Bifurcation (HB) point. The generalized transmissibility is utilized to assess the efficacy of vibration suppression. The various vibration suppression efficiency regions are created by superimposing the vibration suppression efficiency maps and bifurcation maps. The influence of PNES parameters on the vibration suppression region is investigated. The results indicate that this method can effectively evaluate the bifurcation boundary and vibration suppression performance of PMNES.

Keywords: nonlinear energy sink; energy harvesting; bifurcation boundary; vibration suppression

Check for updates

Academic Editor: Bosko Rasuo

Received: 17 December 2025
Revised: 15 January 2026
Accepted: 18 January 2026
Published: 27 January 2026

Copyright: © 2026 by the authors. Licensee MDPI, Basel, Switzerland. This article is an open access article distributed under the terms and conditions of the Creative Commons Attribution (CC BY) license.

1. Introduction

Vibration is a ubiquitous phenomenon in engineering systems, and excessive structural vibration can induce fatigue, resonance, and even catastrophic failures [1,2]. This problem is particularly acute in aerospace engineering, where lightweight and highly flexible structures—such as aircraft wings, POP, satellite solar panels, launch vehicle fairings, and spacecraft appendages—are frequently subjected to complex dynamic loads, including engine-induced harmonic excitations, aerodynamic flutter, launch acoustic loads, and orbital disturbances. Uncontrolled vibrations can severely impair structural integrity, pointing accuracy, payload functionality, and overall mission lifespan. Therefore, efficient vibration suppression technologies are essential for ensuring the safety, reliability, and performance of aerospace equipment [3]. Linear dynamic absorbers remain the most widely adopted devices for structural vibration control [4]. Although linear dampers can effectively mitigate vibrations near their tuned frequency, their inherently narrow suppression bandwidth significantly restricts their performance in the broadband and variable-frequency excitation environments typical of aerospace applications. The integration of mechanics and nonlinear dynamics has led to the emergence of various advanced vibration control strategies [5]. A prominent example is Targeted Energy Transfer (TET), achieved by incorporating nonlinear stiffness into conventional linear dampers [6,7]. The resulting Nonlinear Energy Sink (NES) leverages this mechanism to irreversibly transfer energy from the primary structure to an auxiliary mass, thereby enabling broadband vibration attenuation. Owing to its wide operational bandwidth, robust performance, and minimal added mass, the NES has found extensive application in aerospace vibration suppression as well as in general vibration control scenarios encompassing both attenuation [8] and isolation [9,10]. Experimental and numerical investigations have revealed that the dynamic response of NES-equipped systems is highly sensitive to parameter variations, exhibiting distinct regimes such as steady-state periodic responses, weakly modulated responses, and strongly modulated responses (SMR) [11,12].

To further optimize NES performance, numerous enhanced configurations incorporating cubic stiffness elements have been proposed. Notable examples include parallel-type NES composed of multiple nonlinear unit cells connected in parallel [13], series-type NES formed by serially coupling bistable and monostable elements [14], sectional NES designs that introduce nonlinearity through piecewise stiffness characteristics [15,16], and rotational NES implementations in which nonlinear restoring forces arise from bearing-supported rotational motion [17]. The pronounced cubic nonlinearity inherent in these configurations gives rise to rich dynamic behaviors, even in ostensibly simple structural layouts [18].These nonlinear phenomena can be harnessed to improve vibration mitigation—for instance, Hopf bifurcations near resonance can be exploited for efficient vibration suppression [19], and SMR regimes have been demonstrated to outperform traditional steady-state responses in attenuation effectiveness [20]. However, certain nonlinear features may be detrimental; for example, high-amplitude response branches associated with circular-frequency "islands" in the low-frequency domain can compromise system performance [18,21].

Liu et al. [22] demonstrated that by coupling two inclined linear spring–damper elements, one can generate pronounced geometric nonlinear stiffness and nonlinear damping effects. Their results further indicate that increasing the initial inclination angle can suppress or even eliminate undesirable high-amplitude steady-state responses. Employing the Euler–Bernoulli beam theory and the harmonic balance method, Moslemi et al. [23] modeled a translating beam and systematically examined how beam velocity, damping ratio, damper stiffness coefficient, excitation frequency, and external force amplitude influence the onset of strong modulation response, saddle-node bifurcation, and Hopf bifurcation. Zang et al. [24] investigated the dynamics of a lever-type nonlinear energy well attached to

a spacecraft under harmonic excitation, employing an incremental harmonic balance (IHB) method combined with arc-length continuation to trace closed-loop separation frequency response curves. Building on these foundational studies, Ding and Chen have offered a comprehensive perspective on NES-based vibration suppression, significantly informing the present work. In their investigation of tuned nonlinear energy sinks (TNES) under simple harmonic excitation, Ding and Chen [25] employed Runge–Kutta time-domain numerical integration to analyze the system dynamics, revealing that Hopf-induced strongly modulated responses (SMRs) significantly enhance TNES damping performance, while higher mass ratios alleviate unfavorable effects associated with circular-frequency islands and saddle-node bifurcation curves near resonance. Ding et al. [26] further elucidated the response characteristics of coupled NES–linear oscillator systems under harmonic loading by leveraging the Newmark–Newton iterative time-integration method, together with the CX-A, multi-scale perturbation, and Runge–Kutta (RK) methods, to identify optimal excitation frequency and amplitude conditions for effective vibration suppression.

Chen et al. [27] proposed a nonlinear two-stage vibration isolation system composed of dual linear springs, conventional linear isolators, and supplementary horizontal springs, achieving enhanced displacement transmission reduction and capturing rich nonlinear dynamics at higher frequencies. Shen et al. [28] introduced an innovative NES configuration integrating both inertial and ground-stiffness elements, optimizing its parameters via an H_∞ criterion and a multi-objective Grey Wolf algorithm to suppress high-branch responses typically observed in cubic-stiffness NESs. Geng et al. [29] provided analytical solutions for a grounding-type NES and validated their predictions experimentally, demonstrating excellent agreement. Extending the analysis of viscoelastic effects, Moslemi et al. [30] applied the Burgers model to reveal that increased viscoelastic damping can eliminate instabilities and attenuate high-branch responses in nonlinear oscillators. In a recent development, Li et al. [31] designed a lightweight strongly nonlinear damper for impact suppression in a nine-layer linear structure, achieving not only efficient energy dissipation but also redistribution of energy across structural modes. Zhang et al. [32] positioned an NES at the periphery of an elastic beam to attenuate vibrations and introduced an approximate analytical method for steady-state response, corroborated by numerical simulations; their findings have important implications for elastic structures with nonlinear boundary conditions and for the broader adoption of nonlinear dampers. Gourch et al. [33] utilized advanced averaging techniques to derive modulation equations, map the SMR existence domain, and develop optimization strategies that avoid resonance-curve separation while enabling SMR. Chen et al. [34] proposed a variable-potential bistable NES coupled with electromagnetic energy harvesters, dynamically lowering the potential barrier of the bistable NES to reduce excitation thresholds for chaotic and high-stress responses. Finally, Gomez et al. [35] employed numerical optimization to identify optimal NES parameters and provided explicit formulae for achieving peak performance.

In recent years, a variety of electromechanical energy harvesters, including piezoelectric devices [36,37], electromagnetic transducers [38–41], metamaterial-based converters [42], electrostatic converters [43], and triboelectric systems [44,45] have been extensively investigated for converting ambient vibrational energy into electrical power. NES has a wider frequency range and more efficient vibration absorption effect compared to DVA, exhibit broader effective bandwidth and higher vibration attenuation efficiency; therefore, integrating NESs with piezoelectric transduction is particularly attractive for enhancing energy harvesting performance. By integrating these energy-conversion mechanisms into NES, a portion of the vibrational energy absorbed by the NES can be harvested as electricity, thereby enabling the dual functions of vibration attenuation and power generation for the primary structure [46,47]. Subsequent investigations have deepened our understanding

of these multifunctional systems. Kremer and Liu et al. [48] studied an enhanced NES design that achieves simultaneous vibration suppression and energy harvesting. They demonstrated that low intrinsic mechanical damping facilitates efficient energy transfer, yielding characteristic nonlinear phenomena such as SMR and amplitude hopping. Remeck et al. [49,50] analyzed high-frequency dynamic instabilities and pulse-excitation scenarios, reporting increased energy-harvest efficiency alongside improved vibration attenuation in both simulations and experiments. Zhou et al. [51] optimized a two-degree-of-freedom electromagnetic harvester employing magnetic levitation, attaining a peak output power of 4.6 mW across a broad rotational-speed region. Xu et al. [52] investigated a piezoelectric beam under harmonic forcing, finding a no-load output voltage nearly three times greater than that of a conventional PMNES configuration. Bai et al. [53] introduced a hybrid electromagnetic-frictional energy harvester with conversion efficiencies exceeding 70% over multiple frequency bands. Xiong et al. [54] examined the performance of an NES-based inertial harvester under harmonic excitation, demonstrating effective power collection over a wide frequency spectrum while concurrently reducing transmitted forces. Finally, Tian et al. [55] applied a magnetostrictive NES to suppress aeroelastic vibrations in a hypersonic flow environment, showing that strategic variation in installation position, auxiliary mass, damping, and stiffness parameters can significantly enhance both vibration mitigation and energy-utilization efficiency.

Despite significant advances in vibration suppression for aerospace structures, existing research remains limited in delineating the external excitation frequency domain and amplitude thresholds required for effective suppression, particularly lacking in-depth investigations into the influence of PMNES parameters. Current studies predominantly focus on single-degree-of-freedom aerospace systems, with relatively few addressing two-degree-of-freedom configurations, especially regarding multi-degree-of-freedom bifurcation boundaries. This study systematically investigates the vibration suppression and energy harvesting behavior of a Piezoelectric–Monostable Nonlinear Energy Sink (PMNES) coupled with a two-degree-of-freedom primary structure through a combination of analytical analysis and numerical simulations. The objective is to elucidate how nonlinearity-induced bifurcation mechanisms influence vibration suppression and energy transfer processes, rather than to perform a comparative evaluation of energy harvesting efficiency. Within this framework, energy harvesting responses are employed to clarify the relationship between bifurcation regions and variations in electrical output, highlighting the role of nonlinear dynamics in energy transfer behavior. The effects of key PMNES parameters, including damping, mass, and cubic stiffness, on the vibration suppression regions in the ω–A maps are systematically examined. The results demonstrate that the proposed approach provides an effective means for evaluating bifurcation boundaries and vibration suppression performance of the PMNES.

2. Theoretical Model

2.1. Electromechanical Coupling Dynamics Model

This section focuses on a set of force electric coupling control equations to study the vibration suppression performance and energy harvesting efficiency of PMNES integrated into the main structure of a series 2-DOF spacecraft. The two-degree-of-freedom primary structure investigated in this study is not intended as a detailed physical model of any specific aerospace component, but rather an equivalent low-order lumped-parameter dynamical model employed to abstractly represent the dominant low-frequency dynamic behavior of flexible aerospace structures. By adopting a mass–spring–damper formulation, the model preserves physical interpretability while providing a representative analytical framework for investigating the nonlinear dynamic mechanisms and vibration suppression

performance of the proposed PMNES. A simplified dynamic model of the coupled system is illustrated in Figure 1. In this modeling framework, the concentrated masses of the first and second primary structures are denoted by m_1 and m_2, respectively, while m_3 represents the mass of the nonlinear device, i.e., PMNES. The first primary structure is characterized by linear stiffness k_1 and linear damping c_1, and the second primary structure is modeled with linear stiffness k_2 and linear damping c_2. As a nonlinear absorber, PMNES introduces essential nonlinearity into the system via a cubic nonlinear stiffness k_3, while its linear damping is described by c_3. The device is coupled with a piezoelectric transduction subsystem responsible for converting mechanical vibration energy into electrical energy. The electromechanical subsystem is modeled using the following key parameters: a resistive load R, a piezoelectric coupling coefficient θ (indicating the strength of electromechanical interaction), the linear stiffness of the piezoelectric layer K_p, and the equivalent capacitance C_p (representing energy storage capability). The voltage output from the piezoelectric device is denoted by $x_4(t)$. This external force triggers the system response, enabling detailed analysis of its vibration mitigation and energy harvesting characteristics.

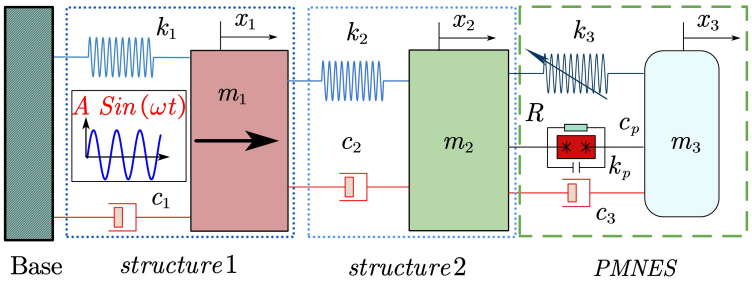


Figure 1. Schematic diagram of two-degree-of-freedom main structure coupled with PMNES.

The primary structure is driven by an external input, formulated as a sinusoidal force $A\,\mathrm{Sin}\,\omega$t, where ω represents the angular frequency applied to the first stage of the structure. This harmonic excitation mimics typical vibrational loading conditions frequently encountered in engineering structural systems.

The mechanical system is developed based on Newton's second law, whereas the electrical dynamics are described using Kirchhoff's current law. By coupling the mechanical and electrical domains via the piezoelectric interaction, the governing equations of the system's electromechanical response can be derived as follows:

$$\begin{aligned}
&m_1\ddot{x}_1 + c_1(\dot{x}_1) + c_2(\dot{x}_1 - \dot{x}_2) + k_1(x_1) + k_2(x_1 - x_2) = A\sin\omega t \\
&m_2\ddot{x}_2 + c_2(\dot{x}_2 - \dot{x}_1) + c_3(\dot{x}_2 - \dot{x}_3) + k_2(x_2 - x_1) + k_3(x_2 - x_3)^3 + k_p(x_2 - x_3) - \theta(x_4) = 0 \\
&m_3\ddot{x}_3 + c_3(\dot{x}_3 - \dot{x}_2) + k_3(x_3 - x_2)^3 + k_p(x_3 - x_2) + \theta(x_4) = 0 \\
&-\theta(\dot{x}_3 - \dot{x}_2) + C_p(\dot{x}_4) + \frac{1}{R}(x_4) = 0
\end{aligned} \tag{1}$$

A dimensionless time scale is introduced to reduce the formulation complexity, defined by

$$\overline{\tau} = t\sqrt{\frac{k_1}{m_1}}; \overline{x}_i = x_i \tag{2}$$

Hereafter, we use t and x_i to represent the dimensionless variables $\overline{\tau}$ and $\overline{x}_i$ for brevity. The non-dimensionalized form of Equation (1) is then

$$\begin{aligned}
&\ddot{x}_1 + \lambda_1\dot{x}_1 + \lambda_2(\dot{x}_1 - \dot{x}_2) + x_1 + k_{21}(x_1 - x_2) = A_1 \sin\omega t \\
&M_2\ddot{x}_2 + \lambda_2(\dot{x}_2 - \dot{x}_1) + \lambda_3(\dot{x}_2 - \dot{x}_3) + k_{21}(x_2 - x_1) + k_{31}(x_2 - x_3)^3 + k_{p1}(x_2 - x_3) - \theta_n(x_4) = 0; \\
&M_3\ddot{x}_3 + \lambda_3(\dot{x}_3 - \dot{x}_2) + k_{31}(x_3 - x_2)^3 + k_{p1}(x_2 - x_3) + \theta_n(x_4) = 0 \\
&-\theta_{\mathrm{m}}(\dot{x}_3 - \dot{x}_2) + C_{pp}(\dot{x}_4) + \frac{1}{R_{n1}}(x_4) = 0
\end{aligned} \tag{3}$$

In this context, $(\dot{})$ represents differentiation with respect to the dimensionless time $\overline{\tau}$. The corresponding non-dimensional parameters in Equation (3) are given by

$$\begin{aligned}
&\lambda_1 = \sqrt{\frac{1}{k_1 m_1}}c_1; \lambda_2 = \sqrt{\frac{1}{k_1 m_1}}c_2; \lambda_3 = \sqrt{\frac{1}{k_1 m_1}}c_3; k_{21} = \frac{k_2}{k_1}; k_{31} = \frac{k_3}{k_1}; k_{p1} = \frac{k_p}{k_1}; \\
&M_2 = \frac{m_2}{m_1}; M_3 = \frac{m_3}{m_1}; \theta_n = \frac{\theta}{k_1}; \theta_m = \sqrt{\frac{k_1}{m_1}}\frac{\theta}{k_1}; R_{n1} = k_1 R; C_{pp} = \sqrt{\frac{k_1}{m_1}}\frac{C_p}{k_1}; A_1 = \frac{A}{k_1};
\end{aligned} \tag{4}$$

The relevant parameters of the two-degree-of-freedom primary structure coupled with PMNES are summarized in Table 1 [56].

Table 1. The parameters of the two-degree-of-freedom main structure coupled with PMNES.

Parameter	Value	Parameter	Value	Parameter	Value	Parameter	Value
m_1 (kg)	2200	C_p (F)	1×10^{-4}	k_1 (N/m)	5.2×10^5	c_1 (N s/m)	500
m_2 (kg)	1400	R (Ω)	1×10^6	k_2 (N/m)	1.3×10^6	c_2 (N s/m)	1000
m_3 (kg)	70	θ (C/m)	1×10^{-1}	k_3 (N/m^3)	2.6×10^5	c_3 (N s/m)	50
K_p (N/m)	100	A (N)	1.8×10^3	–	–	–	–

To quantify the vibration suppression performance of the main structure coupled with an NES, it is crucial to compare it to the response of the system in the absence of the NES. The governing equations for the system without the NES are presented below:

$$\begin{aligned}
&\ddot{x}_1 + \lambda_1\dot{x}_1 + \lambda_2(\dot{x}_1 - \dot{x}_2) + x_1 + k_{21}(x_1 - x_2) = A_1 \cos(\omega \mathrm{t}) \\
&M_2\ddot{x}_2 + \lambda_2(\dot{x}_2 - \dot{x}_1) + k_{21}(x_2 - x_1) = 0
\end{aligned} \tag{5}$$

The particular solution for the steady-state response of the system is assumed to have the following form:

$$\begin{aligned}
x_1 &= \rho_{11}\sin(\omega t) + \rho_{21}\cos(\omega t) \\
x_2 &= \rho_{12}\sin(\omega t) + \rho_{22}\cos(\omega t)
\end{aligned} \tag{6}$$

The following expression represents a stable analytical solution, derived through rigorous mathematical analysis, which accurately characterizes the behavior of the system under study:

$$x_{Without-NES} = \sqrt{{\rho_{11}}^2 + {\rho_{21}}^2} = A_1\sqrt{\frac{a_1}{-2\omega^2 k_{21} M_2 a_2 + k_{21}^2 a_3 + \omega^2 a_4}}; \tag{7}$$

$x_{Without-NES}$: Main structure 1 amplitude without nes. where

$$\begin{aligned} a_1 &= k_{21}^2 - 2\omega^2 k_{21} M_2 + \omega^4 M_2^2 + \omega^2 \lambda_2^2; \\ a_2 &= \left(-1+\omega^2\right)^2 + \omega^2\left(-1+\omega^2\right) M_2 + \omega^2 \lambda_1^2; \\ a_3 &= \left(-1+\omega^2\right)^2 + 2\omega^2\left(-1+\omega^2\right) M_2 + \omega^4 M_2^2 + \omega^2 \lambda_1^2; \\ a_4 &= \begin{pmatrix} 2\omega^2\left(-1+\omega^2\right) M_2 \lambda_2^2 + \left(\left(-1+\omega^2\right)^2 + \omega^2 \lambda_1^2\right)\lambda_2^2 \\ \\ +M_2^2\left(\omega^2 - 2\omega^4 + \omega^6 + \omega^4 \lambda_1^2 + 2\omega^4 \lambda_1 \lambda_2 + \omega^4 \lambda_2^2\right) \end{pmatrix}; \end{aligned} \tag{8}$$

For the NES-coupled dual-degree-of-freedom main structure, the inherent nonlinearities prevent the derivation of a closed-form analytical solution. However, the amplitude response of the main structure can be accurately obtained by solving the governing equation, Equation (3). As shown in Figure 2, the flowchart illustrates the procedure for identifying the worst-case amplitude, which serves as the foundation for determining the critical conditions for optimal vibration suppression and energy harvesting in the PMNES system. The analysis begins with the following application of the CX-A method to Equation (3) to extract the slow-flow dynamics:

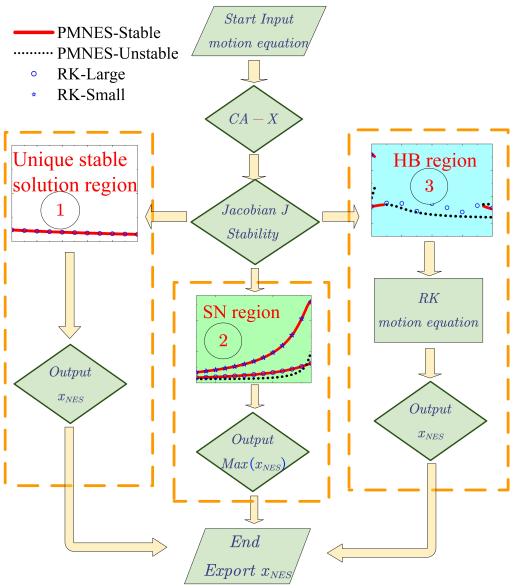


Figure 2. Flowchart Modified for solving maximum amplitude and its stability.

- **Branch 1 (Unique stable solution region).** Branch 1 corresponds to a stable region in Figure 3. This branch is located away from the natural frequency. All eigenvalues of the Jacobian matrix have negative real parts in this region, indicating stable steady-state responses. The system exhibits relatively simple nonlinear behavior.
- **Branch 2 (SN region).** Branch 2 represents the saddle-node (SN) region in Figure 3. In this region, the Jacobian analysis indicates the coexistence of multiple equilibrium solutions, leading to both high-amplitude and low-amplitude stable responses. The maximum stable response on this branch is identified as the most unfavorable condition for vibration suppression.
- **Branch 3 (HB region).** Branch 3 corresponds to the Hopf region in Figure 3. In this case, a pair of complex-conjugate eigenvalues of the Jacobian matrix crosses the imaginary axis, indicating a Hopf bifurcation. Strongly modulated responses (SMR) occur near the natural frequency, and the system exhibits complex nonlinear dynamics.

The response amplitude in this region is obtained using the Runge–Kutta (RK) method to solve Equation (3).

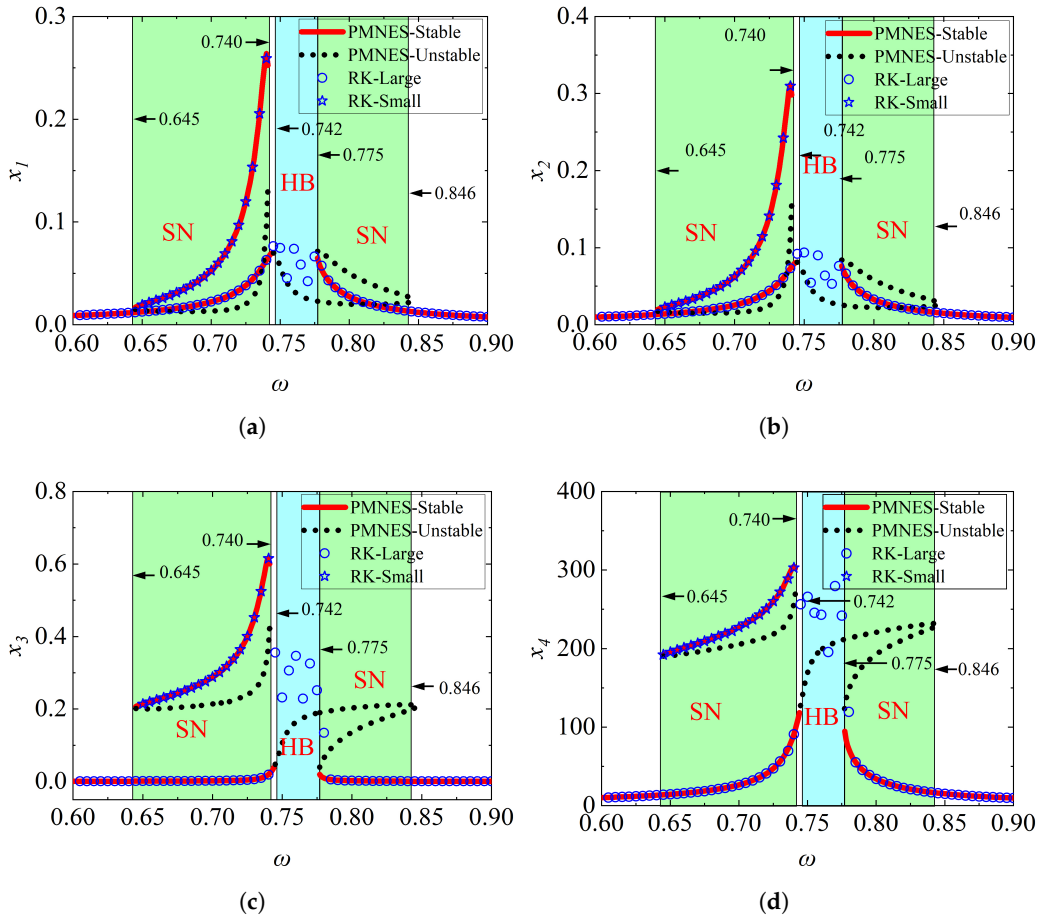


Figure 3. Amplitude–circular frequency response plots of the 2-DOFS PMNES system. (All amplitudes in the figure are dimensionless.) (**a**) Amplitude–circular frequency curve of main structure 1. (**b**) Amplitude–circular frequency curve of main structure 2. (**c**) Amplitude–circular frequency curves of PMNES. (**d**) Amplitude–circular frequency curves of voltage.

Stability is assessed using an enhanced algorithm that is based on the Jacobian matrix of the slow-flow system. This enhanced algorithm provides a clear and systematic procedure to identify bifurcation points and classify dynamic regimes. Specifically, for each equilibrium solution obtained from the CX-A method, the Jacobian matrix is constructed and its eigenvalues are evaluated to determine stability. Provides an accurate characterization of worst-case vibration conditions in the PMNES system. Based on this criterion, three distinct response branches are identified, as shown in Figures 2 and 3.

It should be noted that the CX-A approach adopted in this study is developed under the assumption that the system response remains close to a periodic motion with slowly varying amplitudes. Under this assumption, the CX-A method is used to identify the onset of instability and to estimate Hopf bifurcation boundaries. The method is not intended to describe the strongly modulated or non-periodic responses that may arise after the Hopf bifurcation. Such post-bifurcation dynamics are analyzed through direct numerical simulations in this work. Therefore, using the aforementioned algorithm, the maximum amplitude response and corresponding stability for each external excitation frequency can be accurately determined. These results form the basis for evaluating the vibration suppression efficiency. The generalized transmissibility is employed to

characterize the vibration mitigation effect of NES under base excitation. The vibration suppression efficiency η of NES is defined as [57]

$$\eta = \frac{x_{Without-NES} - x_{NES}}{x_{Without-NES}} \times 100\% \tag{9}$$

where $x_{Without-NES}$ is the amplitude of the main structure 1 coupled to PMNES and is the amplitude of the main structure 1 without coupling to PMNES.

2.2. Approximate Analytical Solution

CX-A proves highly effective in obtaining the steady-state solutions of nonlinear systems, making it particularly suitable for analyzing peak responses and stability characteristics during frequency sweep processes. It accurately captures the bifurcation structure of the system, providing valuable insights into the connection and isolation behaviors among different response branches. This capability enables CX-A to identify both high-branch and low-branch responses, and to precisely locate the maximum amplitude response state under various external excitation conditions [13]. In this study, the displacements, velocities, and accelerations of the two primary structures and the PMNES are expressed using complex variables, as shown below:

$$\begin{aligned} x_i &= \frac{\psi_i - {\psi_1}^*}{2j\omega} \\ \dot{x}_i &= \frac{1}{2}(\psi_i + {\psi_i}^*); \\ \ddot{x}_i &= \dot{\psi}_i - \frac{1}{2}j\omega(\psi_i + {\psi_i}^*); \end{aligned} \tag{10}$$

where $j = (-1)^{1/2}$, $i = 1, 2, 3, 4$.

The overdot symbol denotes differentiation with respect to time t. The complex conjugate of ψ_i is denoted by ψ_i^*, where $i = 1, 2, 3, 4$. The current study focuses on the 1:1:1 internal resonance between the two-degree-of-freedom main structure and the NES oscillator. This resonance condition is introduced as a representative theoretical assumption to investigate the fundamental dynamic behavior of the PMNES, including nonlinear energy transfer, bifurcation evolution, and strongly modulated responses. It should be noted that this assumption does not imply that real aerospace structures strictly satisfy an exact 1:1:1 frequency ratio, but rather provides an idealized framework for analyzing nonlinear coupling mechanisms. To facilitate the analytical treatment of the system's dynamic response, each state variable is expressed using a complex variable formulation. Specifically, the response is decomposed into a rapidly oscillating term, $e^{j\omega t}$, and a slowly varying complex amplitude component, φ_i ($i = 1, 2, 3, 4$), such that

$$\psi_i(t) = \varphi_i e^{j\omega t} \tag{11}$$

By substituting Equations (10) and (11) into Equation (3) and applying the method of averaging to filter out the rapidly oscillating components, the slow-scale dynamics of the system can be derived. In this process, higher-order harmonics such as $e^{j2\omega t}$ and $e^{j3\omega t}$ are neglected, as their contributions to the slow-flow behavior are insignificant. Consequently, the reduced-order slow-flow equations governing the system dynamics are obtained as

$$
\begin{aligned}
&(\dot{\varphi}_1 + jw\varphi_1 - \frac{1}{2}jw\varphi_1) + \frac{1}{2}\lambda_1\varphi_1 + \frac{1}{2}\lambda_2(\varphi_1 - \varphi_2) - \frac{1}{2w}j\varphi_1 - \frac{1}{2w}jk_{21}(\varphi_1 - \varphi_2) = A_1\frac{1}{2}\\
&M_2(\dot{\varphi}_2 + jw\varphi_2 - \frac{1}{2}jw\varphi_2) + \frac{1}{2}\lambda_2(\varphi_2 - \varphi_1) + \frac{1}{2}\lambda_3(\varphi_2 - \varphi_3) - \frac{1}{2w}jk_{21}(\varphi_2 - \varphi_1) -\\
&\frac{3}{8w^3}k_{31}j|\varphi_2 - \varphi_3|^2(\varphi_2 - \varphi_3) - \frac{1}{2w}jk_{p1}(\varphi_2 - \varphi_3) + \frac{1}{2w}j\theta_n\varphi_4 = 0\\
&M_3(\dot{\varphi}_3 + jw\varphi_3 - \frac{1}{2}jw\varphi_3) + \frac{1}{2}\lambda_3(\varphi_3 - \varphi_2) - \frac{3}{8w^3}k_{31}j|\varphi_3 - \varphi_2|^2(\varphi_3 - \varphi_2)\\
&- \frac{1}{2w}jk_{p1}(\varphi_3 - \varphi_2) - \frac{1}{2w}j\theta_n\varphi_4 = 0\\
&-\theta_m\frac{1}{2}(\varphi_3 - \varphi_2) + C_{p1}\left(\frac{1}{2}\varphi_4\right) - \frac{1}{R_{n1}}\frac{1}{2w}j\varphi_4 = 0
\end{aligned}
\tag{12}
$$

To facilitate the analytical process and reduce computational complexity, the displacement differences between subsystems are collectively represented using newly introduced variables. This substitution allows the avoidance of direct expansion and manipulation of cubic nonlinear terms, thereby simplifying the formulation. The introduced variables are defined as follows:

$$
u_1 = \varphi_1 - \varphi_2; u_2 = \varphi_2 - \varphi_3; u_3 = \varphi_1 + M_2\varphi_2 + M_3\varphi_3\,; U = \varphi_4; \tag{13}
$$

here, u_1 denotes the relative displacement between Main Structure 1 and Main Structure 2, while u_2 represents the relative displacement between Main Structure 2 and the PMNES. The variable u_3 corresponds to the motion of the system's center of mass, and U denotes the control voltage.

Substituting Equation (13) into Equation (12) yields the reformulated governing equations of motion for the system as

$$
\begin{aligned}
&\dot{u}_1 + (\Gamma_{11} + \Gamma_{11j})u_1 + (\Gamma_{12} + \Gamma_{12j})u_2 + (\Gamma_{13} + \Gamma_{13j})u_3 + \Gamma_{14j}|u_2|^2u_2 + \frac{-j}{2wM_2}U\theta_n - \frac{1}{2}A_1 = 0\\
&\dot{u}_2 + (\Gamma_{21} + \Gamma_{21j})u_1 + (\Gamma_{22} + \Gamma_{22j})u_2 + \Gamma_{23j}|u_2|^2u_2 + \left(\frac{1}{M_2} + \frac{1}{M_3}\right)\frac{j}{2w}U\theta_n = 0\\
&\dot{u}_3 + (\Gamma_{31} + \Gamma_{31j})u_1 + (\Gamma_{32} + \Gamma_{32j})u_2 + (\Gamma_{33} + \Gamma_{33j})u_3 - \frac{1}{2}A_1 = 0\\
&\frac{UC_{pp}}{2} - j\frac{U}{2wR_n} + \frac{\theta_m}{2}u_2 = 0
\end{aligned}
\tag{14}
$$

here, Γab and Γab$j$ (where a $= 1, 2, 3$ and b $= 1, 2, 3$) represent the real and imaginary components, respectively, as detailed in Appendix A.1.

The non-zero constant particular solution of Equation (14) represents the system's steady-state periodic response. To derive this solution, the time derivatives of the state variables are set to zero, i.e., $\dot{u}_1 = \dot{u}_2 = \dot{u}_3 = 0$. Additionally, the complex amplitudes are expressed in polar form to facilitate the analysis, as follows:

$$
u_1 = \rho_1 e^{j\theta_1}; u_2 = \rho_2 e^{j\theta_2}; u_3 = \rho_3 e^{j\theta_3}; U = \rho_4 e^{j\theta_4}; \tag{15}
$$

In this context, ρ_1, ρ_2, ρ_3, and ρ_4 denote the slowly varying amplitude envelopes associated with Main Structure 1, Main Structure 2, the NES oscillator, and the output voltage, respectively. Similarly, θ_1, θ_2, θ_3, and θ_4 represent their corresponding phase variables.

Substituting Equation (15) into Equation (14), and separating the resulting expressions into real and imaginary parts, yields a system of algebraic equations. Solving

this system simultaneously provides the steady-state amplitude and phase responses for each subsystem.

$$\begin{aligned}
&\left(\Gamma_{11}+\Gamma_{11j}\right)\rho_1(\cos\theta_1+j\sin\theta_1)+\left(\Gamma_{12}+\Gamma_{12j}\right)\rho_2(\cos\theta_2+j\sin\theta_2)\\
&+\left(\Gamma_{13}+\Gamma_{13j}\right)\rho_3(\cos\theta_3+j\sin\theta_3)+\Gamma_{14j}{\rho^3}_2(\cos\theta_2+j\sin\theta_2)\\
&+\frac{-j}{2wM_2}\rho_4(\cos\theta_4+j\sin\theta_4)\theta_n-\frac{1}{2}A_1=0\\
&\left(\Gamma_{21}+\Gamma_{21j}\right)\rho_1(\cos\theta_1+j\sin\theta_1)+\left(\Gamma_{22}+\Gamma_{22j}\right)\rho_2(\cos\theta_2+j\sin\theta_2)\\
&+\Gamma_{23j}{\rho^3}_2(\cos\theta_2+j\sin\theta_2)+\left(\frac{1}{M_2}+\frac{1}{M_3}\right)\frac{j}{2w}\rho_4(\cos\theta_4+j\sin\theta_4)\theta_n=0\\
&\left(\Gamma_{31}+\Gamma_{31j}\right)\rho_1(\cos\theta_1+j\sin\theta_1)+\left(\Gamma_{32}+\Gamma_{32j}\right)\rho_2(\cos\theta_2+j\sin\theta_2)\\
&+\left(\Gamma_{33}+\Gamma_{33j}\right)\rho_3(\cos\theta_3+j\sin\theta_3)-\frac{1}{2}A_1=0\\
&\frac{C_{pp}}{2}\rho_4(\cos\theta_4+j\sin\theta_4)-j\frac{1}{2wR_n}\rho_4(\cos\theta_4+j\sin\theta_4)+\frac{\theta_m}{2}\rho_2(\cos\theta_2+j\sin\theta_2)=0
\end{aligned}\tag{16}$$

Solving the derived algebraic system allows for precise determination of the system's unknown parameters. Accordingly, analytical forms of the responses for both main structures, the PMNES and the voltage output, are obtained, forming the foundation for subsequent analysis and interpretation.

$$\begin{aligned}
x_1&=\frac{\rho_3\,\mathrm{Sin}(\omega t+\theta_3)+\rho_1\,\mathrm{Sin}(\omega t+\theta_1)(M_2+M_3)+\rho_2\,\mathrm{Sin}(\omega t+\theta_2)M_3}{\omega(1+M_2+M_3)};\\
x_2&=\frac{\rho_3\,\mathrm{Sin}(\omega t+\theta_3)-\rho_1\,\mathrm{Sin}(\omega t+\theta_1)+\rho_2\,\mathrm{Sin}(\omega t+\theta_2)M_3}{\omega(1+M_2+M_3)};\\
x_3&=\frac{\rho_3\,\mathrm{Sin}(\omega t+\theta_3)-\rho_1\,\mathrm{Sin}(\omega t+\theta_1)-\rho_2\,\mathrm{Sin}(\omega t+\theta_2)(1+M_2)}{\omega(1+M_2+M_3)};
\end{aligned}\tag{17}$$

The piezoelectric control equations are decoupled, and their real and imaginary components are separated for further analysis.

$$U=\left(\Gamma U+\Gamma U_j\right)u_2,\Gamma U=\frac{-\theta_m\omega^2{R_n}^2C_{pp}}{\left(C_{pp}\omega R_n\right)^2+1},\Gamma U_j=\frac{-j\theta_m\omega R_n}{\left(C_{pp}\omega R_n\right)^2+1};\tag{18}$$

The piezoelectric control equation (Equation (18)) is coupled with the structural control equation (Equation (14)) to derive a new control equation as follows:

$$\begin{aligned}
&\dot{u}_1+\left(\Gamma_{11}+\Gamma_{11j}\right)u_1+\left(\Gamma_{12}+\Gamma_{12j}\right)u_2+\left(\Gamma_{13}+\Gamma_{13j}\right)u_3+\Gamma_{14j}|u_2|^2u_2+\frac{-j}{2\omega M_2}\left(\Gamma U+\Gamma U_j\right)u_2-\frac{1}{2}A_1=0\\
&\dot{u}_2+\left(\Gamma_{21}+\Gamma_{21j}\right)u_1+\left(\Gamma_{22}+\Gamma_{22j}\right)u_2+\Gamma_{23j}|u_2|^2u_2+\left(\frac{1}{M_2}+\frac{1}{M_3}\right)\frac{j}{2\Gamma}\left(\Gamma U+\Gamma U_j\right)u_2=0\\
&\dot{u}_3+\left(\Gamma_{31}+\Gamma_{31j}\right)u_1+\left(\Gamma_{32}+\Gamma_{32j}\right)u_2+\left(\Gamma_{33}+\Gamma_{33j}\right)u_3-\frac{1}{2}A_1=0
\end{aligned}\tag{19}$$

The stability of the equilibrium point is evaluated by analyzing the perturbed system in the vicinity of the equilibrium. The corresponding steady-state response of the system can be represented as

$$u_i=u_{i0}+\delta_i,i=1,2,3\tag{20}$$

where δ_i denotes the perturbation term. Substituting Equation (20) into Equation (19) yields the linearized equations with respect to δ_i as

$$\begin{aligned}
&\dot{\delta}_1 + (\Gamma_{11} + \Gamma_{11j})\delta_1 + (\Gamma_{12} + \Gamma_{12j})\delta_2 + (\Gamma_{13} + \Gamma_{13j})\delta_3 \\
&+ \Gamma_{14j}\left[|u_{20}|^2\delta_2 + (u_{20})^2\bar{\delta}_2 + |u_{20}|^2\delta_2\right] + \frac{-j}{2\omega M_2}\theta_n(\Gamma U + \Gamma U_j)\delta_2 - \frac{1}{2}A_1 = 0 \\
&\dot{\delta}_2 + (\Gamma_{21} + \Gamma_{21j})\delta_1 + (\Gamma_{22} + \Gamma_{22j})\delta_2 \\
&+ \Gamma_{23j}\left[|u_{20}|^2\delta_2 + (u_{20})^2\bar{\delta}_2 + |u_{20}|^2\delta_2\right] + \left(\frac{1}{M_2} + \frac{1}{M_3}\right)\frac{j}{2\omega}\theta_n(\Gamma U + \Gamma U_j)\delta_2 = 0 \\
&\dot{\delta}_3 + (\Gamma_{31} + \Gamma_{31j})\delta_1 + (\Gamma_{32} + \Gamma_{32j})\delta_2 + (\Gamma_{33} + \Gamma_{33j})\delta_3 - \frac{1}{2}A_1 = 0
\end{aligned} \tag{21}$$

To derive the Jacobian matrix for stability analysis, δ_i is expressed in the following complex form:

$$\delta_i = p_i + jq_i, i = 1, 2, 3 \tag{22}$$

By substituting Equation (22) into Equation (21) and separating the resulting expression into its real and imaginary parts, we obtain

$$\begin{aligned}
\dot{p}_1 &= \frac{A_1}{2} - \Gamma_{11}p_1 - \Gamma_{12}p_2 - \frac{\theta_n\Gamma U_j p_2}{2\omega M_2} - \Gamma_{13}p_3 + \Gamma_{11}jq_1 + \Gamma_{12j}q_2 - \frac{\theta_n\Gamma U q_2}{2\omega M_2} \\
&+ \Gamma_{13j}q_3 + 2\cos\theta_2\sin\theta_2\Gamma_{14j}p_2\rho_2^2 + 2\Gamma_{14j}q_2\rho_2^2 - (\cos\theta_2)^2\Gamma_{14j}q_2\rho_2^2 + (\sin\theta_2)^2\Gamma_{14j}q_2\rho_2^2 \\
\dot{q}_1 &= -\Gamma_{11j}p_1 - \Gamma_{12j}p_2 + \frac{\theta_n\Gamma U p_2}{2\omega M_2} - \Gamma_{13j}p_3 - \Gamma_{11}q_1 - \Gamma_{12}q_2 - \frac{\theta_n\Gamma U_j q_2}{2\omega M_2} - \Gamma 13q_3 \\
&- 2\Gamma_{14j}p_2\rho_2^2 - (\cos\theta_2)^2\Gamma_{14j}p_2\rho_2^2 + (\sin\theta_2)^2\Gamma_{14j}p_2\rho_2^2 - 2\cos\theta_2\sin\theta_2\Gamma_{14j}q_2\rho_2^2 \\
\dot{p}_2 &= -\Gamma_{21}p_1 - \Gamma_{22}p_2 + \frac{\theta_n\Gamma U_j p_2}{2\omega M_2} + \frac{\theta_n\Gamma U_j p_2}{2\omega M_3} + \Gamma_{21j}q_1 + \Gamma_{22j}q_2 + \frac{\theta_n\Gamma U q_2}{2\omega M_2} + \frac{\theta_n\Gamma U q_2}{2\omega M_3} \\
&+ 2\cos\theta_2\sin\theta_2\Gamma_{23j}p_2\rho_2^2 + 2\Gamma_{23j}q_2\rho_2^2 - (\cos\theta_2)^2\Gamma_{23j}q_2\rho_2^2 + (\sin\theta_2)^2\Gamma_{23j}q_2\rho_2^2 \\
\dot{q}_2 &= -\Gamma_{21j}p_1 - \Gamma_{22j}p_2 - \frac{\theta_n\Gamma U p_2}{2\omega M_2} - \frac{\theta_n\Gamma U p_2}{2\omega M_3} - \Gamma_{21}q_1 - \Gamma_{22}q_2 + \frac{\theta_n\Gamma U_j q_2}{2\omega M_2} + \frac{\theta_n\Gamma U_j q_2}{2\omega M_3} \\
&- 2\Gamma_{23j}p_2\rho_2^2 - (\cos\theta_2)^2\Gamma_{23j}p_2\rho_2^2 + (\sin\theta_2)^2\Gamma_{23j}p_2\rho_2^2 - 2\cos\theta_2\sin\theta_2\Gamma_{23j}q_2\rho_2^2 \\
\dot{p}_3 &= \frac{A_1}{2} - \Gamma_{31}p_1 - \Gamma_{32}p_2 - \Gamma_{33}p_3 + \Gamma_{31j}q_1 + \Gamma_{32j}q_2 + \Gamma_{33j}q_3 \\
\dot{q}_3 &= -\Gamma_{31j}p_1 - \Gamma_{32j}p_2 - \Gamma_{33j}p_3 - \Gamma_{31}q_1 - \Gamma_{32}q_2 - \Gamma_{33}q_3
\end{aligned} \tag{23}$$

By separating Equation (23) into its real and imaginary components, the Jacobian matrix is obtained. The output response of the PMNES can then be investigated using Lyapunov's stability theory. In particular, the local stability of the equilibrium point is assessed by examining the eigenvalues of the Jacobian matrix $J(\dot{p}_1, \dot{q}_1, \dot{p}_2, \dot{q}_2, \dot{p}_3, \dot{q}_3)$ (Equation (24)). If all eigenvalues possess negative real parts, the equilibrium is locally asymptotically stable. However, the presence of any eigenvalue with a positive real part indicates local instability, as the equilibrium solution diverges.

$$\begin{aligned}
J &= \begin{pmatrix} \left[\frac{\partial\dot{\mathbf{p}}_i}{\partial\mathbf{p}_j}\right]_{3\times3} & \left[\frac{\partial\dot{\mathbf{p}}_i}{\partial\mathbf{q}_j}\right]_{3\times3} \\ \left[\frac{\partial\dot{\mathbf{q}}_i}{\partial\mathbf{p}_j}\right]_{3\times3} & \left[\frac{\partial\dot{\mathbf{q}}_i}{\partial\mathbf{q}_j}\right]_{3\times3} \end{pmatrix} \cdots i, j = 1, 2, 3 \\
\mathbf{p} &= (p_1, p_2, p_3)^T \qquad \mathbf{q} = (q_1, q_2, q_3)^T
\end{aligned} \tag{24}$$

Fixed-point bifurcations play a critical role in shaping the steady-state dynamics of the system. These bifurcations signify transitions between different motion regimes, such as from periodic to quasi-periodic or chaotic behavior. They may arise due to variations in system parameters related to the main structure, the PMNES, or the piezoelectric coupling. By defining $|u_2|^2 = S$, Equation (19) can be simplified to yield the following characteristic equation:

$$\Psi_3 S^3 + \Psi_2 S^2 + \Psi_1 S + \Psi_0 = 0 \tag{25}$$

For the sake of brevity, the detailed forms of Ψ_3, Ψ_2, Ψ_1, and Ψ_0 are provided in Appendix A.2. Equation (25) can be transformed into the following form:

$$Y^3 + pY + q = 0 \tag{26}$$

where

$$\begin{aligned} Y &= Z_2 + \frac{\Psi_2}{3\Psi_3}; \\ p &= \frac{3\Psi_3\Psi_1 - \Psi_2^2}{3\Psi_3^2}; \\ q &= \frac{27\Psi_3^2\Psi_4 - 9\Psi_3\Psi_2\Psi_1 + 2\Psi_2^3}{27\Psi_3^3}; \end{aligned} \tag{27}$$

According to the Cardano discriminant, the bifurcation boundary can be expressed as follows:

$$\Delta = \left(\frac{q}{2}\right)^2 + \left(\frac{p}{3}\right)^3 \tag{28}$$

Equation (25) admits (i) one real root for $\Delta > 0$ (single equilibrium), (ii) three real roots with multiplicity for $\Delta = 0$ (SN bifurcation), and (iii) three distinct real roots for $\Delta < 0$ (multiple equilibria). The bifurcation condition based on Equation (28) is given by

$$\begin{aligned} SN_1 : \left\{ (\Psi_0, \Psi_1, \Psi_2, \Psi_3) \middle| \begin{array}{c} 27\Psi_3^2\Psi_0 + 9\Psi_3\Psi_1\left(-\Psi_2 - \sqrt{\Psi_2^2 - 3\Psi_1\Psi_3}\right) + \\ 3\Psi_2\left(-\Psi_2 - \sqrt{\Psi_2^2 - 3\Psi_1\Psi_3}\right)^2 + \left(-\Psi_2 - \sqrt{\Psi_2^2 - 3\Psi_1\Psi_3}\right)^3 = 0 \end{array} \right\}; \\ SN_2 : \left\{ (\Psi_0, \Psi_1, \Psi_2, \Psi_3) \middle| \begin{array}{c} 27\Psi_3^2\Psi_0 + 9\Psi_3\Psi_1\left(-\Psi_2 + \sqrt{\Psi_2^2 - 3\Psi_1\Psi_3}\right) + \\ 3\Psi_2\left(-\Psi_2 + \sqrt{\Psi_2^2 - 3\Psi_1\Psi_3}\right)^2 + \left(-\Psi_2 + \sqrt{\Psi_2^2 - 3\Psi_1\Psi_3}\right)^3 = 0 \end{array} \right\}; \end{aligned} \tag{29}$$

As the two-dimensional parameter plane evolves, the coefficients in the standard form of the saddle-node (SN) bifurcation may degenerate. This degeneration requires the introduction of additional bifurcation conditions to account for the emergence of a new bifurcation—namely, the codimension-two cusp bifurcation.

$$\text{cusp:} \left\{ (\Psi_0, \Psi_1, \Psi_2, \Psi_3) \middle| 27\Psi_3^2\Psi_0 + 9\Psi_3\Psi_1(-\Psi_2) + 2\Psi_2^3 = 0 \right\} \tag{30}$$

3. Results and Discussion

3.1. Verification of Approximate Solutions

In this section, the CX-A method is utilized to obtain the displacement amplitude of the system as well as the voltage response of the sensing device. The system's stability under varying external excitation frequencies is evaluated by constructing the Jacobian

matrix. The accuracy of the CX-A method is further validated through comparison with the RK method. The parameters used in the analysis are summarized in Table 1.

As illustrated in Figure 3, the amplitude–ω response curves of PMNES near its first-order natural frequency are presented. The ordinates $x1$ to $x4$ represent the responses of main structure 1, main structure 2, NES, and voltage, respectively. Bifurcation points, stability types, and instability regions are marked. PMNES-Stable and PMNES-Unstall denote the stable and unstable branches derived from CX-A, while RK-Small and RK-Large refer to RK results with small and large initial conditions. From Figure 3, CX-A and RK predictions match well along the stable branches. In the low-ω region [0.645, 0.740], the intersection of the frequency island and low-energy orbit forms a triple-solution region, consisting of large initial, small initial, and SN solutions. The upper island corresponds to a stable high-amplitude branch (large initial), while the lower edge ends at an SN bifurcation. The coexisting low-energy orbit forms a stable low-amplitude branch (small initial). In Figure 3a,b, a closed loop of stable and unstable branches appears in the high-ω region [0.775, 0.846], bounded by two SNs. Additionally, in the transitional region [0.742, 0.775], an HB occurs. Affected by SMR, CX-A fails to fully capture the amplitude response, resulting in deviations from RK. This indicates CX-A's limitations in predicting SMR-induced modulations near HB.

It should be noted that the roles of the approximate analytical solutions and the numerical solutions are inherently different in stable and unstable regions of the parameter space. In the stable solution regions, the steady-state responses obtained from the approximate analytical method show very good agreement with the numerical results calculated using the fourth-order Runge–Kutta scheme, confirming the validity of the proposed analytical approach. In contrast, in the unstable regions, the two approaches naturally exhibit different characteristics, which is consistent with the fundamental properties of nonlinear dynamical systems. The approximate solutions derived via the CA-X are mainly used to identify equilibrium solutions and assess their stability through the eigenvalues of the Jacobian matrix of the corresponding slow-flow equations, thereby accurately locating instability boundaries. The Runge–Kutta time-domain simulations, on the other hand, are capable of capturing the full nonlinear transient and long-term dynamical behaviors, and thus provide a more faithful representation of the actual system dynamics in unstable regimes. The combined use of analytical and numerical approaches ensures a comprehensive and consistent characterization of the nonlinear dynamics in both stable and unstable regions [58,59].

Figure 4 illustrates the basins of attraction of the system at two representative excitation frequencies, $\omega = 0.695$ and $\omega = 0.72$, obtained from time-domain simulations using the fourth-order Runge–Kutta method. The basins are plotted in the plane of the initial displacement and velocity of Main Structure 1, while the initial conditions of Main Structure 2 and the PMNES are fixed at zero. Different colors indicate convergence to distinct stable periodic solutions with small and large response amplitudes, respectively. At $\omega = 0.695$, the basin structure exhibits a complex interwoven pattern, with both low-amplitude and high-amplitude attractors occupying significant regions of the initial-condition space. This indicates strong multistability and a pronounced sensitivity of the steady-state response to the initial conditions of Main Structure 1. In contrast, at $\omega = 0.72$, the basin corresponding to the large-amplitude response dominates most of the phase space, while the basin of the small-amplitude solution shrinks considerably, reflecting an evolution of the global nonlinear dynamics with increasing excitation frequency. By fixing the initial conditions of Main Structure 2 and the PMNES and varying only the initial conditions of Main Structure 1, different coexisting attractors can be systematically accessed. The basin-of-attraction analysis therefore provides a rational basis for selecting initial conditions in the numerical

simulations. By choosing initial conditions from within the target attraction basin, the convergence of the Runge–Kutta integration to the desired stable solution is ensured, thereby guaranteeing the consistency and reliability of the subsequent bifurcation and time-domain analyses [60].

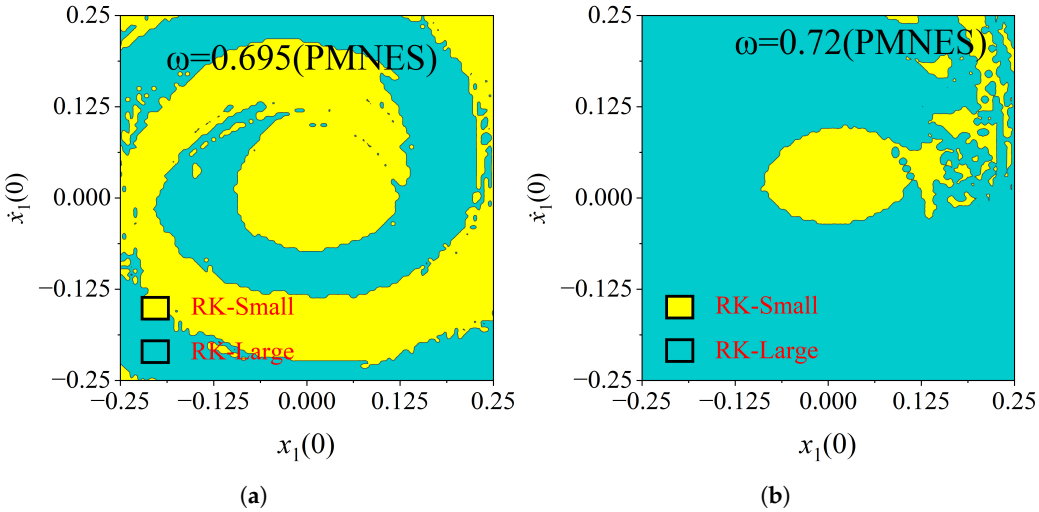


Figure 4. Attractor basin under different external excitation circular frequencies. (**a**) $\omega = 0.695$. (**b**) $\omega = 0.72$.

Figure 5a presents the bifurcation diagram of the vibration amplitude of main structure 1 with respect to ω. An HB occurs within the region [0.742, 0.775], indicating a transition from steady-state periodic motion to SMR. Figure 5b shows the maximum Lyapunov exponent computed from the Jacobian matrix. When the maximum Lyapunov exponent is positive, the system's response becomes unstable, which aligns with the identification of the HB bifurcation regions. The SN regions are identified in [0.645, 0.740] and [0.775, 0.846], which is consistent with the bifurcation behavior shown in Figure 5.

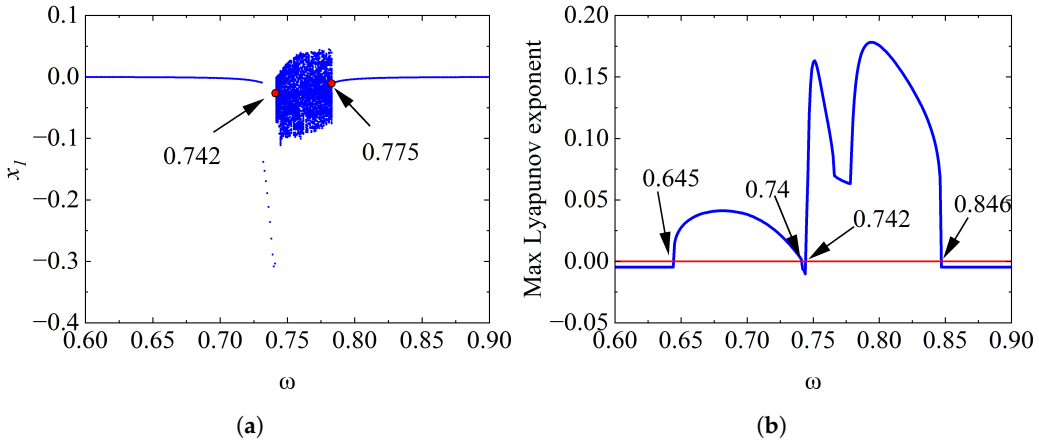


Figure 5. Stability analysis of the 2-DOFS PMNES system. (**a**) Main structure 1 amplitude response. (**b**) Maximum Lyapunov exponent graph.

In the A–ω domain, the SN bifurcation boundary is obtained through analytical expressions, as shown in Figure 6. When the excitation force is set to 1800 N, the boundary intersects both SN regions, namely [0.645, 0.740] and [0.775, 0.846]. The left boundaries are labeled S_{A1} and S_{A2}, while the right boundaries are labeled S_{A3} and S_{A4}. As the excitation frequency increases, the system first enters the low-frequency SN bifurcation region (induced by frequency islands), then transitions into the resonance region (associated

with the system's natural frequency), and eventually enters the high-frequency SN region (induced by softening effects). Each SN region contains multiple approximate solutions, including at least one stable and one unstable branch, consistent with the SN behavior observed in Figure 3. As the system transitions from within an SN region to outside, three fixed points coalesce into one, marking the occurrence of an SN bifurcation. This leads to the disappearance of the multi-solution regime in CX-A, accompanied by the loss of nonlinear dynamic features such as hardening, softening, and frequency island effects. Furthermore, stability transitions cause changes in the system's oscillation mode.

In fact, the normalized form factor of the SN bifurcation gradually deteriorates with the variation in parameters on the two-dimensional plane defined by the external force and the excitation circular frequency. This degradation reflects the increasing complexity and sensitivity of the bifurcation structure in the nonlinear regime. Therefore, to capture the precise local behavior near criticality, the normalized form of the codimension-two cusp bifurcation point must be derived using Equation (30). At the intersection of the two SN bifurcation curves, a codimension-two cusp bifurcation occurs, which subsequently evolves into a single bifurcation curve, marking a topological transition in the system's dynamic response.

In addition, as illustrated in Figure 7a, the threshold of external force required to induce bifurcation is significantly lower in the high-frequency SN region. This indicates that the system is more prone to instability at higher frequencies. Specifically, as the excitation force increases, softening phenomena first occur in the resonance region, followed by the onset of SN bifurcation in the low-frequency region. Further increases in excitation force then trigger frequency island phenomena. This sequential emergence reveals a frequency-dependent bifurcation mechanism and underscores the asymmetric nature of system response under varying excitation conditions.

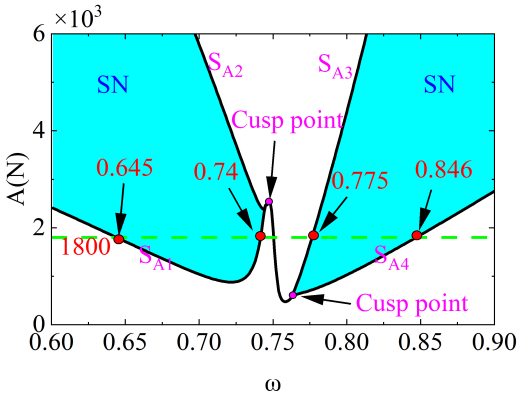


Figure 6. SN bifurcation boundary.

As illustrated in Figure 7, the amplitude–circular frequency response curves of the system are presented under varying external excitation forces. The blue curve represents the amplitude response of the main structure without a PMNES, while the red curve corresponds to the response with a PMNES. As the external force increases, the damping effect imparted by the PMNES becomes increasingly pronounced, as seen in Figure 7a. Near the natural circular frequency, the response curve begins to bend, and an HB occurs, indicating the onset of the SMR phenomenon, where damping around the natural frequency intensifies. When the bending becomes sufficiently pronounced and the external force reaches 900 N, a frequency island emerges in the low-frequency region. With further increases in excitation force (Figure 7b), the effective damping contribution of the PMNES gradually decreases; the frequency island shifts toward the natural circular frequency, and the HB near the natural frequency disappears. Simultaneously, the low-branch curve starts

intersecting the frequency island. At an excitation level of 2700 N, the frequency island coalesces with the main response curve, and the distinct peak within the island ceases to exist, with the global maximum returning to the principal branch. Figure 7c,d show that under higher excitation forces, the primary resonance peak shifts toward lower frequencies, and the SN region expands bilaterally. Although the NES continues to effectively suppress the amplitude near the natural circular frequency beyond a certain force threshold—thus providing significant damping—the emergence of new peaks in the low-frequency region highlights inherent limitations of the NES under high-energy excitations. These results demonstrate that the PMNES can effectively induce SMR under moderate excitation levels, thereby enhancing damping performance near resonance. However, under high-intensity excitation, the appearance of low-frequency islands, the disappearance of HB near resonance, and the formation of secondary peaks must be carefully considered in evaluating NES performance and optimization strategies.

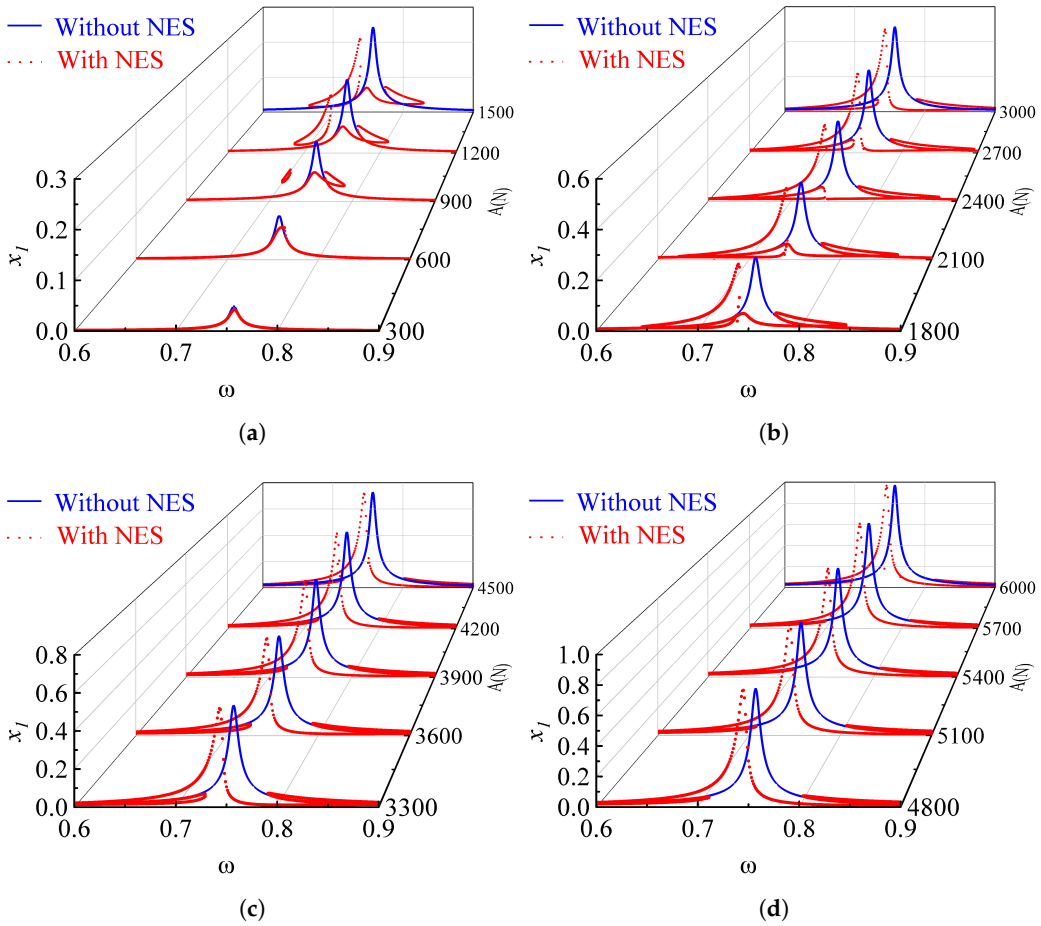


Figure 7. Influence of external exciting force on amplitude. (**a**) 300 N $\leq A(\mathrm{N}) \leq$ 1500 N; (**b**) 1800 N $\leq A(\mathrm{N}) \leq$ 3000 N; (**c**) 3300 N $\leq A(\mathrm{N}) \leq$ 4500 N; (**d**) 4800 N $\leq A(\mathrm{N}) \leq$ 6000 N.

3.2. Influence of PMNES Parameters on Vibration Suppression Region

The system parameters of the PMNES have a substantial impact on the SN bifurcation region, which is closely associated with the effective vibration suppression region (EVSR) across different circular frequency bands. Based on Equations (7) and (9), the vibration suppression efficiency within the bifurcation region is evaluated, and the effects of various parameters on vibration suppression performance over different frequency bands are investigated, as summarized in Table 2. Regions with attenuation efficiency lower than −2% are identified as the amplification area (AAR), indicating a deterioration of vibration suppression performance. Regions exhibiting a small positive attenuation efficiency

slightly greater than 2% are classified as the effective vibration suppression region (EVSR). In the HB region, where the vibration suppression efficiency is much greater than 2%, the corresponding operating domain is defined as the HB vibration suppression region (HBVSR), reflecting strong nonlinear energy dissipation characteristics induced by the Hopf bifurcation. Furthermore, regions with vibration suppression efficiency within the interval [0, 2%] are categorized as the ineffective vibration suppression region I (IVSR-I), while those with efficiency within the interval [−2%, 0] are denoted as the ineffective vibration suppression region II (IVSR-II).

This study investigates the mechanisms governing these vibration suppression regions by analyzing the relationship between the SN region and the HB vibration suppression region, and by exploring the effects of PMNES system parameters on the HB vibration suppression region.

Table 2. Damping efficiency versus bifurcation type.

Working Condition	Symbol	Damping Efficiency	Bifurcation Type
Amplification Area	AAR	Less than −2%	SN bifurcation
Effective Vibration Suppression Region	EVSR	Slightly greater than 2%	
HB Vibration Suppression Region	HBVSR	Much greater than 2%	HB
Ineffective Region I	IVSR-I	[0, 2%]	
Ineffective Region II	IVSR-II	[−2%, 0]	

3.2.1. Mass Ratio Coefficient β

This section investigates the influence of PMNES mass on SN and HBs, with particular emphasis on the system dynamics in the vicinity of the 1:1:1 internal resonance region, as shown in Figure 8. Figure 8a presents the SN bifurcation curves under varying mass ratios, where the horizontal axis denotes the external excitation circular frequency, and the vertical axis corresponds to the external excitation force. To quantify the effect of PMNES mass m_3 on the overall dynamic response of the primary structural system, a mass ratio coefficient $\beta = \frac{m_3}{m_1+m_2} \times 100\%$ is introduced. This dimensionless parameter allows for consistent comparison across different mass configurations. The vibration suppression efficiency and dynamic stability of each point along the SN bifurcation boundary are evaluated using Equations (9), (16) and (23), which provide the necessary metrics for performance assessment. Based on these results, a series of ω–A vibration suppression partition diagrams are constructed to visualize the performance landscape. Figure 8b–d illustrate the ω–A suppression regions corresponding to different values of β, thereby revealing the sensitivity of bifurcation dynamics and suppression effectiveness to changes in PMNES mass.

As demonstrated in Figure 8a, an increase in the mass ratio coefficient leads to a significant expansion of the low-circular-frequency SN region, which also progressively shifts away from the natural circular frequency. In contrast, the high-circular-frequency SN region shows minimal displacement relative to the natural frequency, indicating differing sensitivities of these regions to changes in the mass ratio. As shown in Figure 8b, the boundary between the ineffective vibration suppression region I and the amplitude amplification region is defined by S_{A1}, while the boundary separating the effective vibration suppression region from the ineffective vibration suppression region II is defined by S_{A3}. Notably, the low-circular frequency SN region is entirely contained within the amplitude amplification region, while the high-circular frequency SN region resides entirely within the ineffective vibration suppression region II. These observations suggest that SN bifurcation in the low-circular frequency region plays a predominant role in the adverse effects of vibration, whereas the effective vibration suppression region occupies the middle frequency region.

The HB occurs within the red region, where the PMNES transitions from steady periodic motion to irregular, large-amplitude oscillatory behavior. As a result, the HB vibration suppression region demonstrates effective vibration suppression, although it occupies a relatively small proportion of the overall frequency region. This region is characterized by a specific threshold, and as the external excitation force increases, the HB vibration suppression region gradually diminishes and ultimately disappears.

As illustrated in Figure 8b–d, two prominent phenomena emerge with the increase in the mass ratio coefficient of the PMNES. First, both the effective vibration suppression region and the HB vibration suppression region undergo significant expansion, indicating enhanced suppression capability over a broader dynamic region. Second, the overall bandwidth of vibration suppression becomes wider, suggesting improved damping effectiveness across an extended frequency region. Meanwhile, the low-circular frequency SN region progressively expands and further penetrates into the amplitude amplification region, whereas the high-circular frequency SN region increasingly dominates the ineffective vibration suppression region II. In addition, a new amplitude amplification region emerges near the bifurcation boundary S_{A3}. It is noteworthy that, as the PMNES mass ratio increases, the threshold of external excitation force required to trigger both SN and HBs also increases.

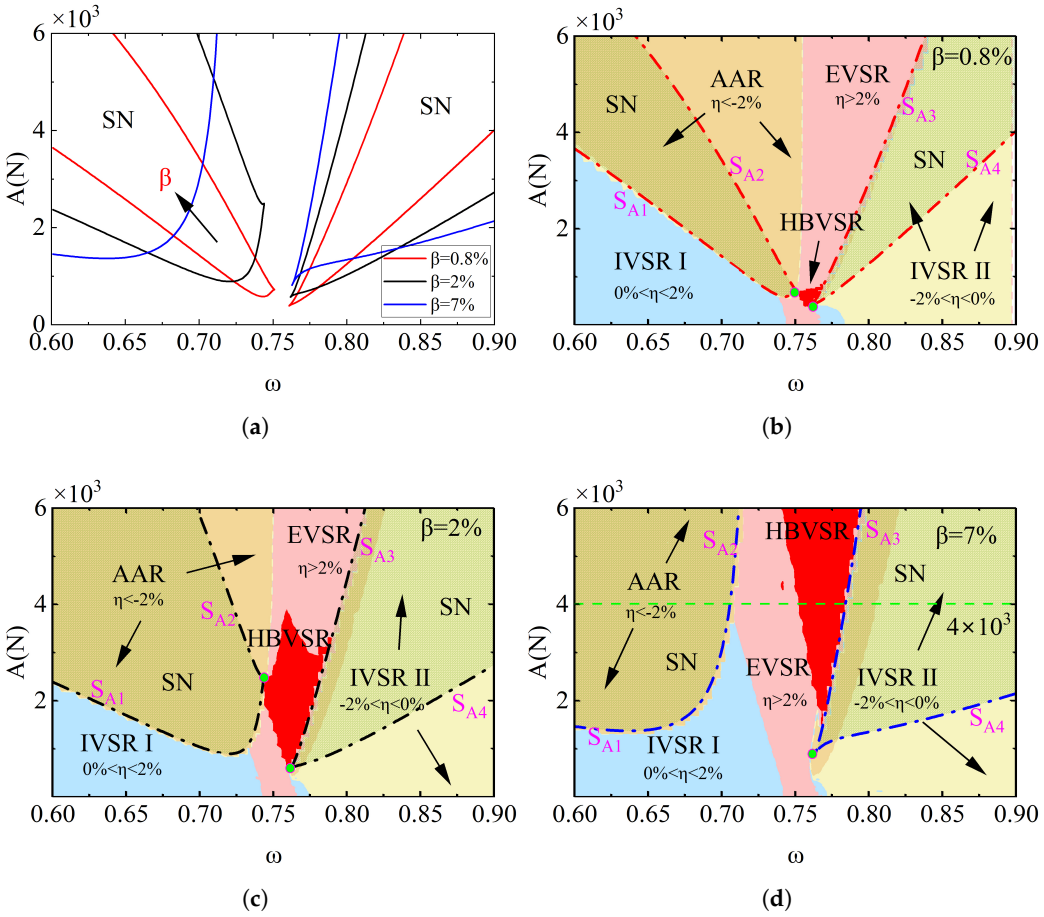


Figure 8. SN bifurcation diagram and ω–A vibration suppression partition diagram under different mass ratio coefficients β. (**a**) SN bifurcation with different mass ratio coefficients; (**b**) $\beta = 0.8\%$; (**c**) $\beta = 2\%$; (**d**) $\beta = 7\%$.

In order to facilitate a more thorough analysis of the aforementioned dynamic behavior, as shown in Figure 8d, the external force of 4×10^3 and the mass ratio coefficient of 7% are used to obtain a new amplitude–circular frequency curve as shown in Figure 9, and the circular frequency of 0.74 in the effective vibration suppression region and the circular

frequency of 0.76 in the HB vibration suppression region are chosen for comparison. The ordinate x_1, x_2, x_3 and x_4 represent the response of main structure 1, main structure 2, NES and stress, respectively. Figure 9a,b display the response comparison of main structures 1 and 2 with and without PMNES, showing clear suppression of the circular frequency near the natural circular frequency. As indicated in Figure 9c,d, PMNES has a strong vibration suppression and energy harvesting effect near the natural circular frequency. From the comparison, it is obvious that the amplitude amplification region on the left is caused by the high branch response of the circular frequency island. The curve on the right side of the natural circular frequency breaks away from the original main curve path due to excessive bending and becomes the amplitude amplification region. As illustrated in Figure 9a,b, in the invalid vibration suppression region II, the main structure system is coupled with PMNES, and the amplitude response hardly changes.

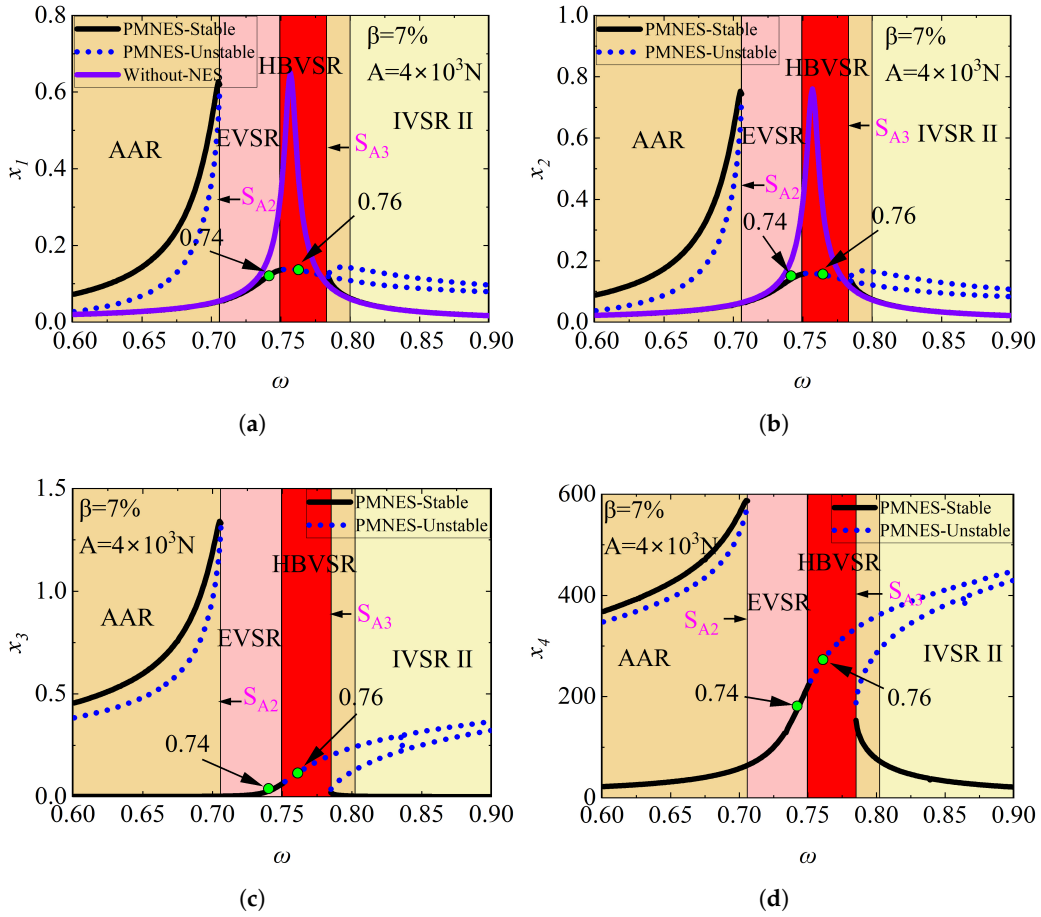


Figure 9. Amplitude–circular frequency response plots of the 2-DOFS PMNES system; $\beta = 7\%$, $A = 4 \times 10^3$ N. (All amplitudes in the figure are dimensionless.) (**a**) Amplitude–circular frequency curve of main structure 1. (**b**) Amplitude–circular frequency curve of main structure 2. (**c**) Amplitude–circular frequency curves of PMNES. (**d**) Amplitude–circular frequency curves of voltage.

As illustrated in Figure 9, the vibration suppression efficiency at frequencies of 0.74 and 0.76 is particularly pronounced, thus necessitating a comprehensive investigation into the discrepancy in vibration suppression and energy harvesting mechanisms of vibration reduction. Figure 10 illustrates the time history curves of each part of the system under an external excitation circular frequency of 0.74. The vertical axis x_1, x_2, x_3 and x_4 represents the response of main structure 1, main structure 2, NES and voltage, respectively. As illustrated in Figure 10a,b, the responses of main structure 1 and main structure 2 are in a stable motion state, and the vibration suppression of the main structure is not obvious

after adding PMNES to the system, and the amplitude decreases only slightly. As can be seen in Figure 10c,d, PMNES still undergoes small periodic movements, and the stress only undergoes stable periodic movements.

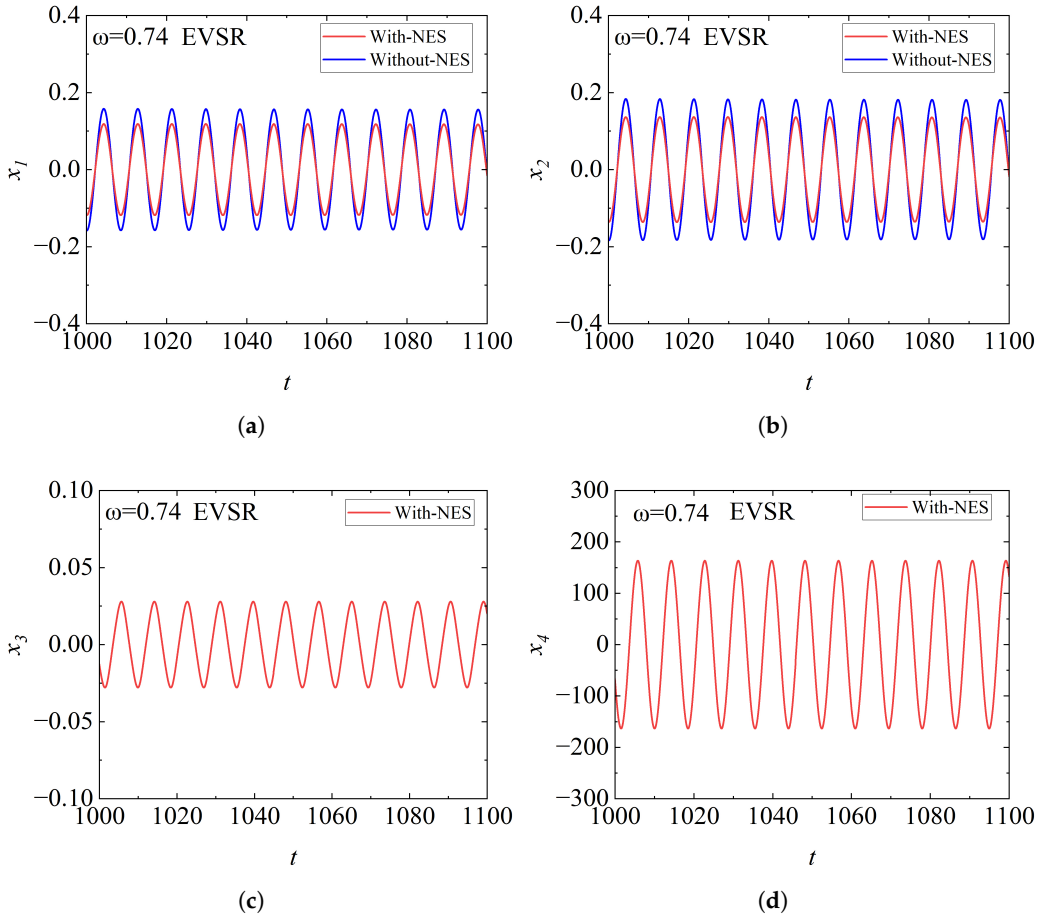


Figure 10. Amplitude–circular frequency response plots of the 2-DOFS PMNES system; $\omega = 0.74$ EVSR. (**a**) Displacement response of main structure 1. (**b**) Displacement response of main structure 2. (**c**) Displacement response of PMNES oscillator. (**d**) Output voltage responses.

Figure 11 illustrates the time histories of various parts of the system under an external excitation circular frequency of 0.76. The vertical axis x_1, x_2, x_3, x_4 represents the response of main structure 1, main structure 2, NES, and voltage response, respectively. Comparing Figures 10 and 11, when the external excitation circular frequency (0.76) is in the HB region, as indicated in Figure 11a,b, the main structures 1 and 2 change from periodic motion to chaotic motion, and their vibrations are effectively suppressed. As demonstrated in Figure 11c,d, PMNES and voltage exhibit substantial, irregular, and violent motions, thereby enhancing the vibration suppression and energy harvesting performance.

The occurrence of HB and SMR phenomenon in the system was observed at an external excitation circular frequency of 0.76. It was found that the system exhibited not only an effective vibration suppression effect, but also a substantial enhancement in energy harvesting efficiency. The effective vibration suppression region was found to demonstrate a certain degree of vibration suppression and energy harvesting efficacy, while the HB vibration suppression region was found to exhibit superior vibration suppression and energy harvesting capabilities.

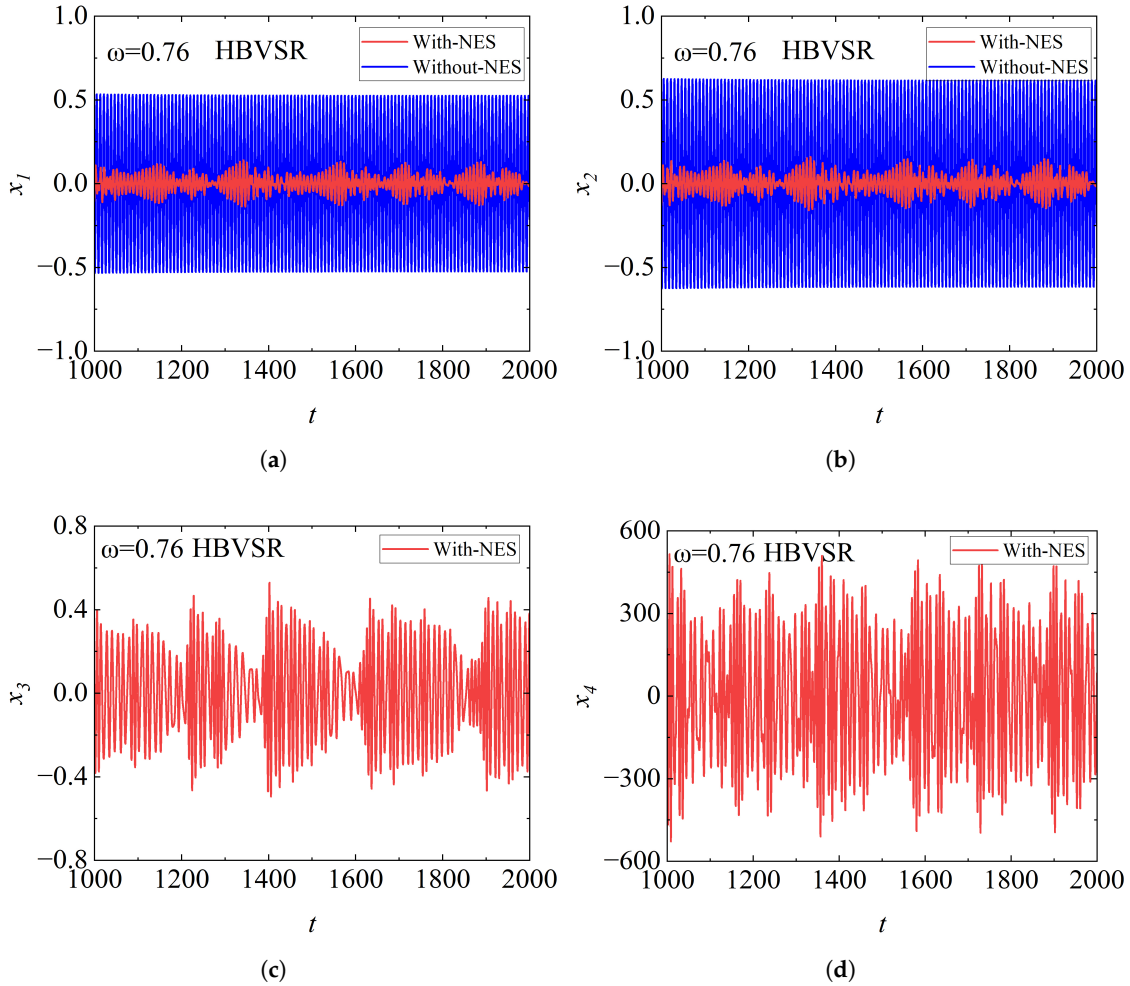


Figure 11. Amplitude–circular frequency response plots of the 2-DOFS PMNES system; $\omega = 0.76$ HBVSR. (**a**) Displacement response of main structure 1. (**b**) Displacement response of main structure 2. (**c**) Displacement response of PMNES oscillator. (**d**) Output voltage responses.

3.2.2. Cubic Stiffness Coefficient K_3

Figure 12a illustrates the bifurcation curve of SN under varying cubic stiffness coefficients k_3. Figure 12b–d show the bifurcation diagrams of $\omega - A$ vibration suppression under different cubic stiffness coefficients k_3. As depicted in Figure 12a, with an increase in the cubic stiffness coefficient, the region of SN bifurcation expands, while the threshold external excitation force required for SN bifurcation decreases. As shown in Figure 12b–d, an amplitude amplification region appears near the boundary of S_{A3}, and with an increase in the cubic stiffness coefficient, the triggering threshold for the HB vibration suppression region decreases. It is evident that the effective vibration suppression region expands, while the HB vibration suppression region contracts. Simultaneously, the amplitude amplification region in the low-circular frequency region increases, while the proportion of the low-circular frequency SN region decreases. The invalid vibration suppression region II continues to shrink, while the proportion of the high-circular frequency SN region increases.

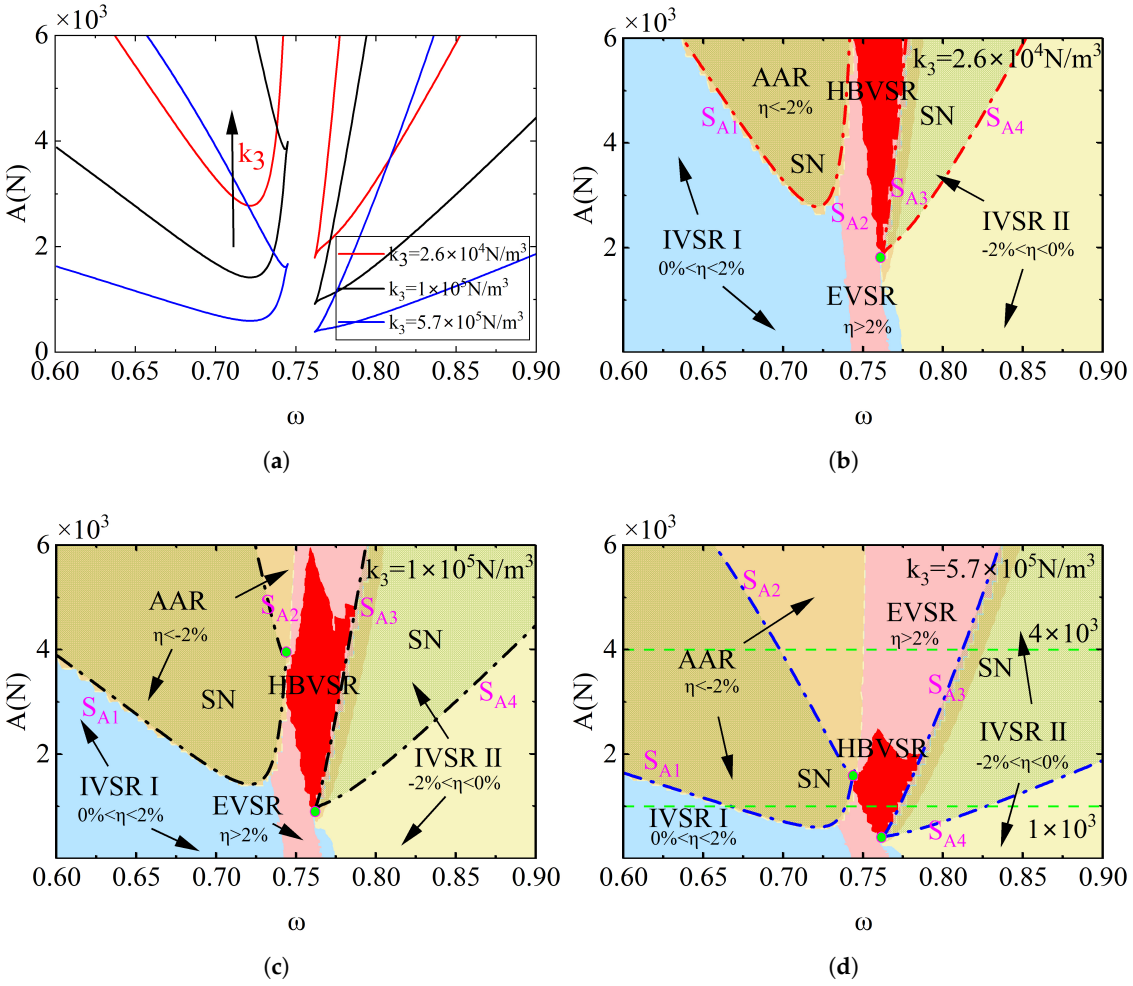


Figure 12. SN bifurcation diagram and ω–A vibration suppression partition diagram under different cubic stiffness coefficients k_3. (**a**) SN bifurcation with different cubic stiffnesses. (**b**) $k_3 = 2.6 \times 10^4$ N/m^3. (**c**) $k_3 = 1 \times 10^5$ N/m^3. (**d**) $k_3 = 5.7 \times 10^5$ N/m^3.

In the low-circular frequency region, for a given excitation circular frequency, an increase in the cubic stiffness coefficient results in the system entering the invalid vibration suppression region I, the low-circular frequency SN bifurcation region, and the amplitude amplification region more rapidly. Conversely, in the high-circular frequency region, an increase in the cubic stiffness coefficient, coupled with an increase in external excitation, accelerates the system's exit from the invalid vibration suppression region II, entry into the high-circular frequency SN bifurcation region, and subsequent re-entry into the amplitude amplification region and the effective vibration suppression region. It is noteworthy that both the void vibration suppression regions I and II exhibit continuous downward movement and contraction.

To better analyze the dynamic behavior, as illustrated in Figure 12d, the external force is set to 4×10^3 and the cubic stiffness coefficient to 5.7×10^5, yielding a new amplitude–circular frequency curve, as shown in Figure 13. Figure 13 presents the amplitude–circular frequency curves of main structure 1, main structure 2, PMNES, and stress, respectively. Figure 13a,b also provide a comparison of the system response with and without PMNES. When the two main structures are coupled with PMNES, new peaks appear in the low-circular frequency region. The peaks of the two systems are shifted, effectively suppressing the amplitude at the natural circular frequency. The circular frequency island is reintegrated with the main curve, and the most unfavorable factor in the amplitude gain region is now

a new peak in the low-circular frequency region. As shown in Figure 13b,c, the peak values of PMNES and voltage have also shifted. Although this shift in peak values is not favorable for vibration suppression, it has little impact on the energy capture capabilities of the system.

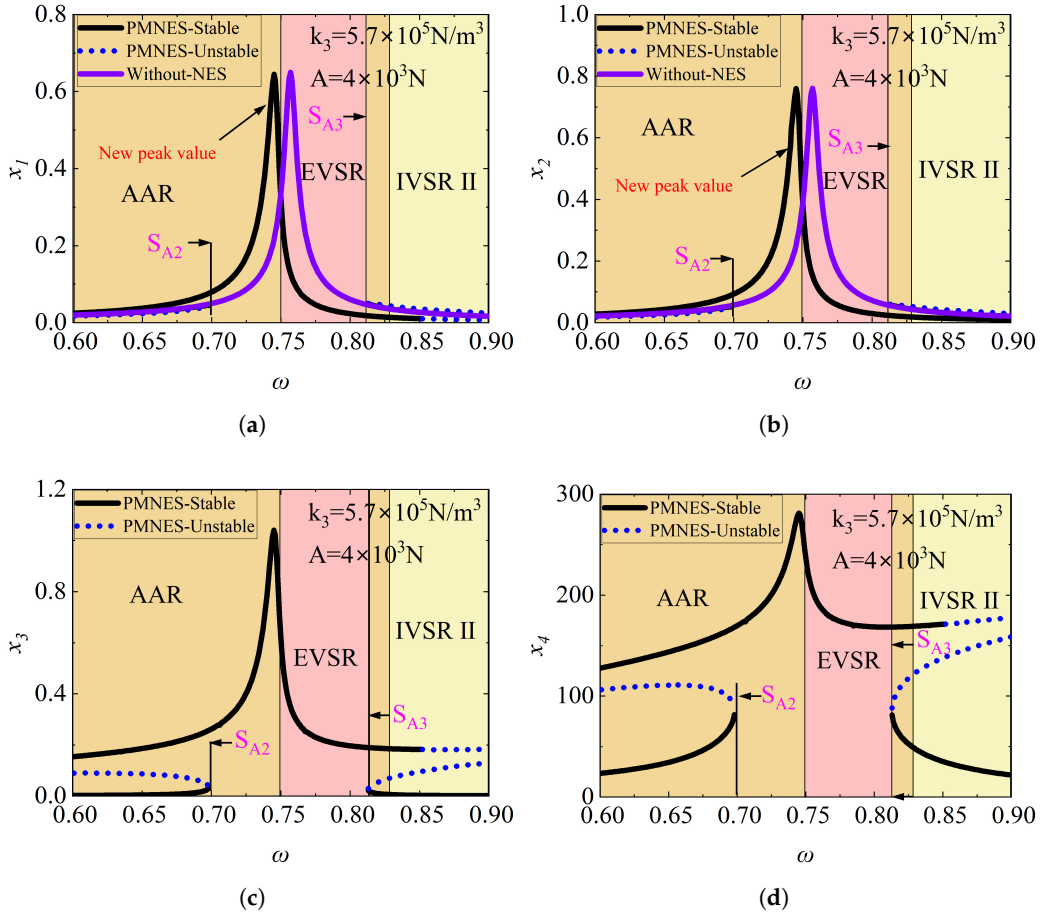


Figure 13. Amplitude–circular frequency response plots of the 2-DOFS PMNES system; $k_3 = 5.7 \times 10^5$ N/m^3, $A = 4 \times 10^3$ N. (All amplitudes in the figure are dimensionless.) (**a**) Amplitude–circular frequency curve of main structure 1. (**b**) Amplitude–circular frequency curve of main structure 2. (**c**) Amplitude–circular frequency curves of PMNES. (**d**) Amplitude–circular frequency curves of voltage.

As demonstrated in Figure 14, when the external excitation force is reduced from 4×10^3 N to 1×10^3 N, the new peak deviation disappears and the frequency island effect emerges, enhancing the energy harvesting capability in the low-frequency region, but it is detrimental to vibration suppression in this region. At this point, HB vibration suppression becomes evident near the natural circular frequency, significantly improving vibration suppression capabilities. However, the high branch response arising from the frequency island effect may result in unfavorable vibration suppression. Although both low and high branches can occur, their responses vary under different external conditions. While external conditions can prevent the transition from the low branch to the high branch, the emergence of the new peak shift phenomenon, as shown in Figure 13, remains inevitable. Therefore, it is imperative in practical engineering design to avoid this new peak shift phenomenon.

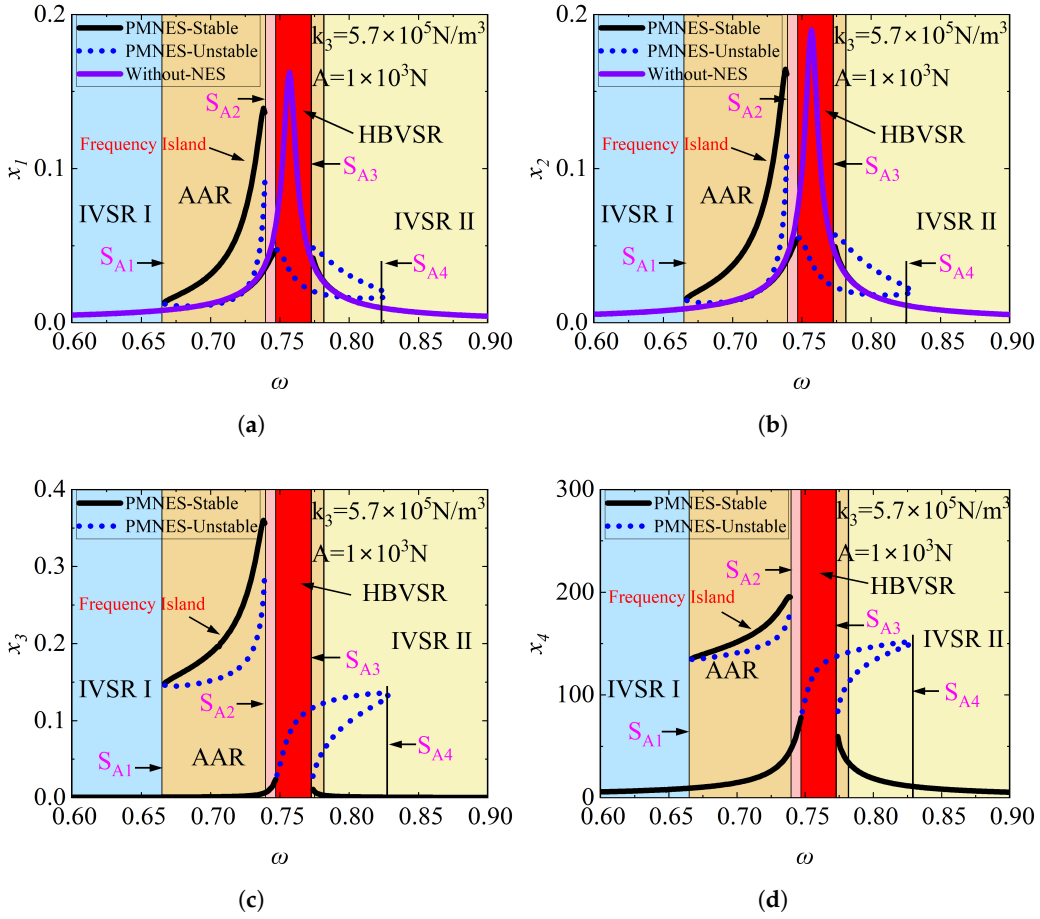


Figure 14. Amplitude–circular frequency response plots of the 2-DOFS PMNES system; $k_3 = 5.7 \times 10^5\,\mathrm{N/m^3}$, $A = 1 \times 10^3\,\mathrm{N}$. (All amplitudes in the figure are dimensionless.) (**a**) Amplitude–circular frequency curve of main structure 1. (**b**) Amplitude–circular frequency curve of main structure 2. (**c**) Amplitude–circular frequency curves of PMNES. (**d**) Amplitude–circular frequency curves of voltage.

By examining all the ω-A vibration suppression partition diagrams, it can be observed that the amplification region on the left side of the amplitude spectrum is caused by two primary factors: the high-branch response of the frequency island and the emergence of a new peak shift in the low-frequency region. As shown in Figure 12d, the codimension-two cusp bifurcation point in the low-frequency region delineates the boundary of external excitation that induces the new peak. When the external excitation force exceeds this cusp point, the system exhibits a new peak shift phenomenon; otherwise, the frequency island effect emerges. The cusp bifurcation point thus serves as a critical external excitation threshold that dictates the transition of dynamical behavior in the low-frequency domain. By applying the established Equation (30), the minimum external excitation force required to trigger this transition can be determined.

3.2.3. Damping Coefficient C_3

Figure 15a presents the saddle-node (SN) bifurcation curves corresponding to various values of the damping coefficient c_3, illustrating how changes in damping influence the system's bifurcation behavior. Figure 15b–d display the ω–A bifurcation diagrams for vibration suppression under different c_3 values, providing a comparative analysis of the system's dynamic response across a region of damping conditions.

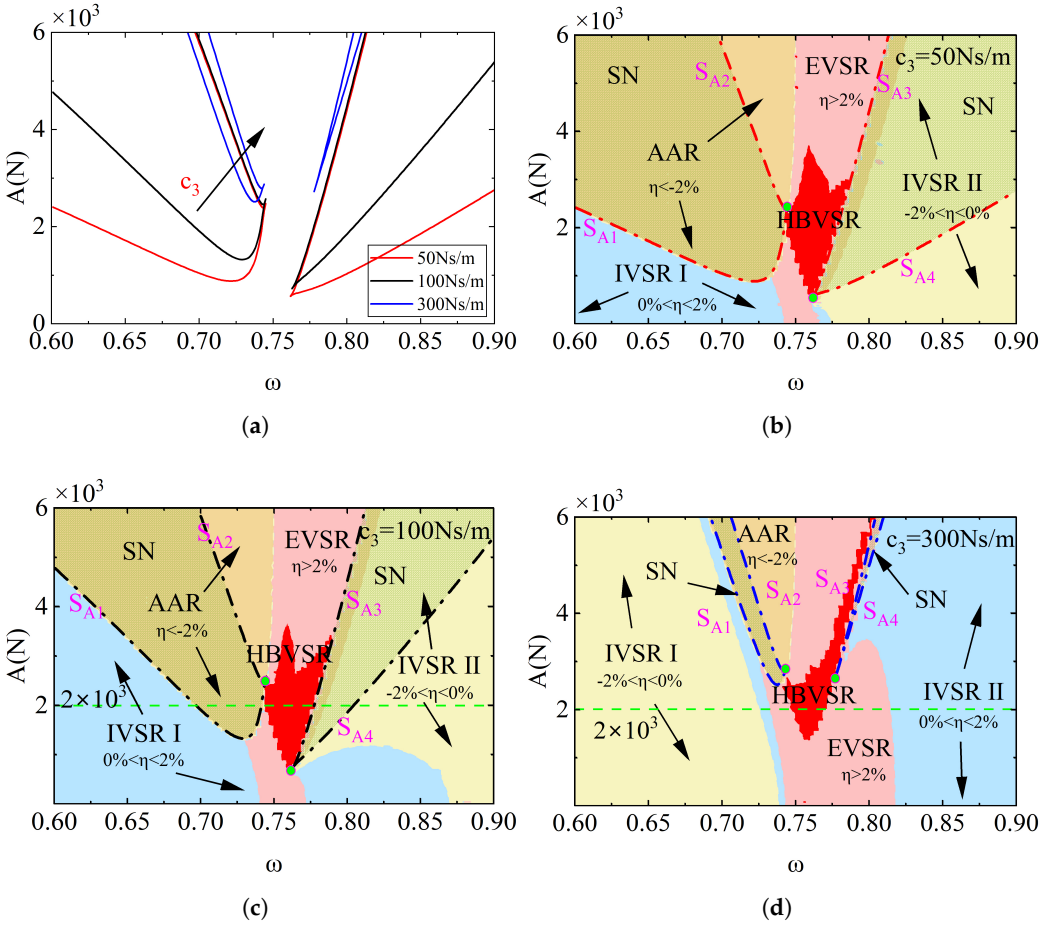


Figure 15. SN bifurcation diagram and ω–A vibration suppression partition diagram under different damping coefficients c_3; (**a**) SN bifurcation under different damping conditions; (**b**) $c_3 = 50\,\mathrm{N\,s/m}$; (**c**) $c_3 = 100\,\mathrm{N\,s/m}$; (**d**) $c_3 = 300\,\mathrm{N\,s/m}$.

As shown in Figure 15a, an increase in the damping coefficient leads to a reduction in the size of the saddle-node (SN) bifurcation region. However, the threshold value of the external excitation force required to trigger SN bifurcation correspondingly increases. This indicates a more stable system response under higher damping conditions. Figure 15b–d further demonstrate that as the damping coefficient increases, the amplitude amplification region progressively narrows. This change effectively suppresses the occurrence of frequency islands and eliminates new peak deviation phenomena, while concurrently broadening the effective vibration suppression region. Notably, when the damping coefficient reaches 300 Ns/m, the SN region at lower circular frequencies shrinks markedly. The invalid vibration suppression region on the left side transitions into what is referred to as invalid vibration suppression region II, whereas the region on the right evolves into invalid vibration suppression region I. Despite adjustments to system parameters, the existence of the invalid vibration suppression region remains invariant. This persistent region is primarily associated with vibration responses occurring far from the resonance frequency region. As the effective suppression zone expands, the amplitude amplification near the bifurcation boundary S_{A3} gradually diminishes, thereby enhancing the broadband vibration suppression performance. Appropriately increasing the damping not only eliminates the frequency island phenomenon but also improves system robustness without compromising suppression efficiency.

To further evaluate the effectiveness and influence of PMNES damping, a comparative analysis was conducted using an external excitation force of 2×10^3, as illustrated in

Figure 15c,d. Figure 16 presents the amplitude–circular frequency response curves for main structure 1, main structure 2, the PMNES device, and the output voltage, based on the conditions described in Figure 15c. Similarly, Figure 17 shows the corresponding amplitude–circular frequency curves under the conditions depicted in Figure 15d. Through this analysis, the role of PMNES damping in shaping broadband vibration suppression characteristics becomes more evident.

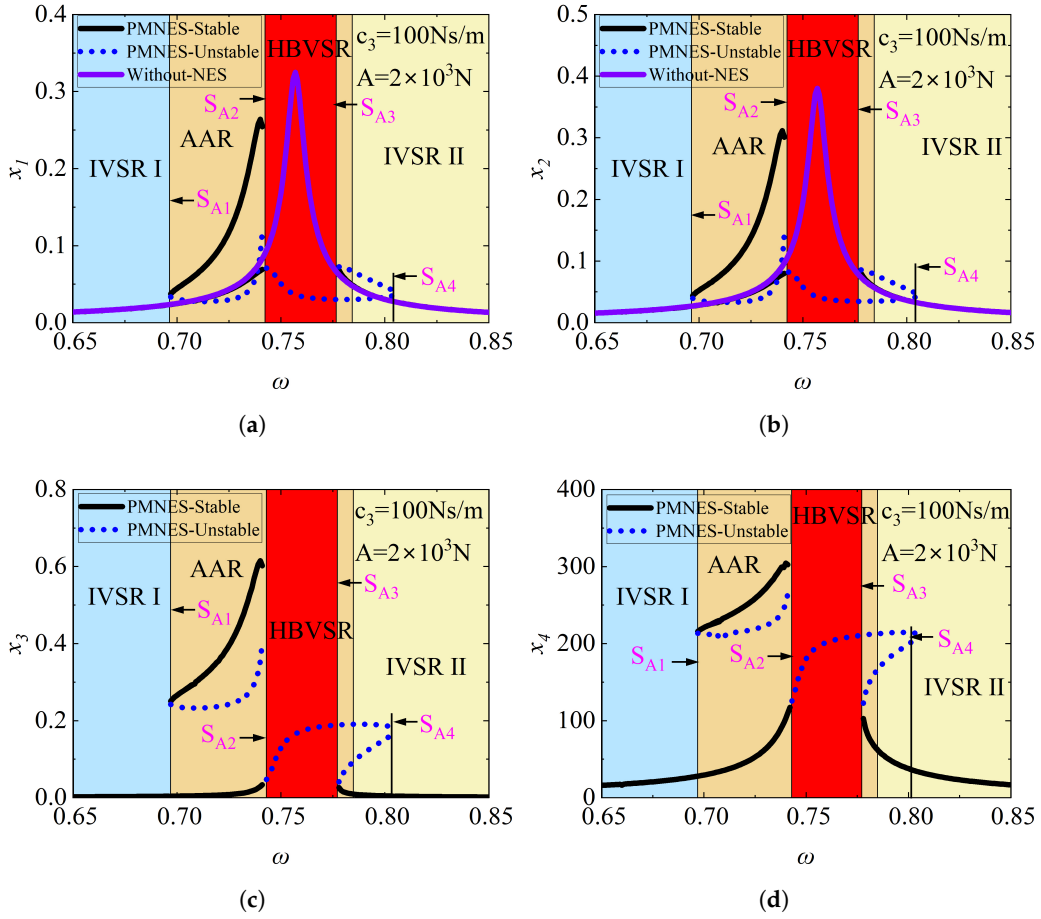


Figure 16. Amplitude–circular frequency response plots of the 2-DOFS PMNES system; $c_3 = 100\,\mathrm{N\,s/m}$, $A = 2 \times 10^3\,\mathrm{N}$. (All amplitudes in the figure are dimensionless.) (**a**) Amplitude–circular frequency curve of main structure 1. (**b**) Amplitude–circular frequency curve of main structure 2. (**c**) Amplitude–circular frequency curves of PMNES. (**d**) Amplitude–circular frequency curves of voltage.

As shown in Figure 16, under the low-damping condition (100 Ns/m), a pronounced frequency island is observed in the low-frequency region. The emergence of the high-branch response significantly reduces the efficiency of vibration suppression, which is detrimental to the overall suppression capability of the system. Around the natural circular frequency, the HBVSR induces the SMR phenomenon, where the suppression effect is both evident and spans a relatively wide frequency region. When the damping is increased to 300 Ns/m, as illustrated in Figure 17, the enhanced damping effect effectively eliminates the formation of frequency islands. However, the HBVSR contracts, leading to a reduction in broadband vibration suppression performance. With the increase in damping, the PMNES system absorbs more mechanical energy, thereby reducing the energy available for conversion into electrical energy. As depicted in Figures 16d and 17d, the voltage response near the natural circular frequency decreases with increased damping, making it infeasible to achieve high voltage output in the low-frequency region.

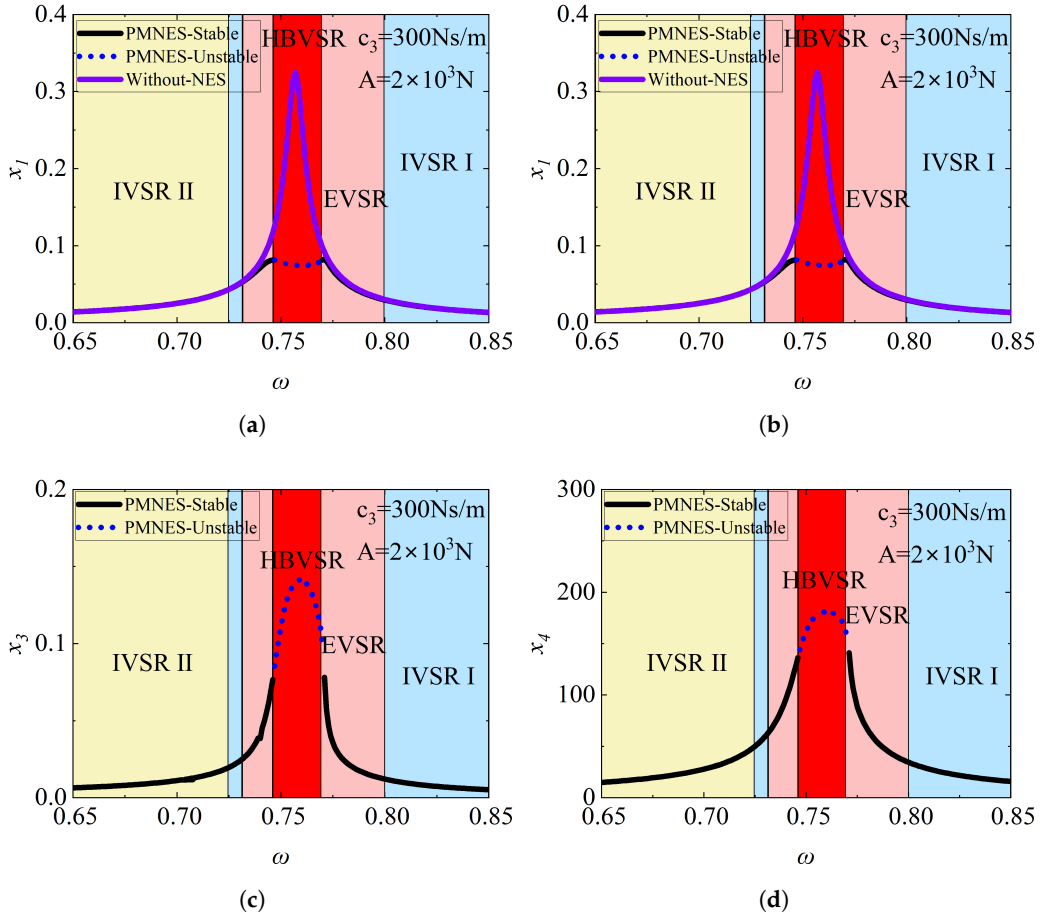


Figure 17. Amplitude–circular frequency response plots of the 2-DOFS PMNES system; $c_3 = 300\,\mathrm{N\,s/m}$, $A = 2 \times 10^3\,\mathrm{N}$. (All amplitudes in the figure are dimensionless.) (**a**) Amplitude–circular frequency curve of main structure 1. (**b**) Amplitude–circular frequency curve of main structure 2. (**c**) Amplitude–circular frequency curves of PMNES. (**d**) Amplitude–circular frequency curves of voltage.

A reduction in PMNES damping results in a prominent high-branch response in the low-frequency domain. Nevertheless, the device exhibits a considerable energy harvesting capability and maintains effective suppression near the natural circular frequency. In contrast, increasing PMNES damping enhances overall vibration suppression performance, albeit at the expense of suppression bandwidth and energy harvesting efficiency. In conclusion, the PMNES system functions not only as a vibration suppressor but also as an effective energy harvester. Increasing the damping coefficient of PMNES enhances the separation between SN and HB excitation thresholds, facilitating easier access to the HB suppression region. This also helps to avoid unfavorable phenomena such as frequency islands and low-frequency peak shifts.

3.3. Bifurcation Behavior Verification

3.3.1. SN Bifurcation at Specific Circular Frequency

In the previous section, the dynamic responses of the system under different external excitation circular frequencies were investigated. This section focuses on the influence of PMNES parameters on the saddle-node (SN) bifurcation behavior at a specific frequency. To better analyze the nonlinear dynamic characteristics near the frequency island, an external excitation circular frequency of 0.65 (in the low-frequency range) is selected for detailed study.

Based on the bifurcation equation (Equation (26)), the bifurcation diagrams are obtained and shown in Figure 18a–c, corresponding to variations in PMNES mass, cubic stiffness coefficient, and damping coefficient, respectively. In each figure, the vertical axis represents the external excitation force. The cyan-shaded region denotes unstable responses, while the outer white region corresponds to stable dynamic behavior. As observed in Figure 18a, as the PMNES mass increases, both the upper and lower bifurcation boundaries shift outward, resulting in an expanded SN bifurcation region. Meanwhile, the threshold value of the external excitation force required to trigger SN bifurcation gradually decreases. This trend is consistent with the results shown in Figure 8. As shown in Figure 18b, increasing the cubic stiffness coefficient of the PMNES leads to a rapid shrinkage of the SN bifurcation region, accompanied by a corresponding decrease in the threshold excitation force. This finding agrees with the conclusion drawn from Figure 12. From Figure 18c, it can be seen that as the damping coefficient of the PMNES increases, the SN bifurcation region significantly contracts. However, in contrast to the effect of stiffness variation, the excitation force threshold in this case increases. When the damping becomes sufficiently large, the SN bifurcation region disappears completely. This phenomenon is highly consistent with the results obtained in Figure 15.

To investigate the relationship between fixed points and SN bifurcations, bifurcation diagrams were constructed by continuously varying the amplitude of the external excitation force. These diagrams reveal the system's steady-state responses as functions of the external excitation amplitude. Figure 18a–c correspond to the parameter planes in Figure 19 as follows: subplots (a), (b), and (c) represent the A-m_3 parameter plane; subplots (d), (e), and (f) correspond to the A-c_3 parameter plane; and subplots (g), (h), and (i) represent the A-k_3 parameter plane. In each subplot, x_1, x_3, and x_4 represent the amplitude of the primary structure 1, the amplitude of the PMNES, and the voltage response, respectively. The horizontal axis denotes the magnitude of the external excitation force. The central multistable region consists of two stable fixed points and one unstable fixed point. The transition between the upper and lower solution branches leads to nontrivial oscillatory responses due to the coexistence of multiple attractors. As the excitation force increases and the system transitions from the multistable region into a monostable region, the system response amplitude grows significantly, which reflects a typical SN bifurcation behavior. These results provide critical insights into how parameter variations influence the coexistence and stability of nonlinear system solutions.

As shown in Figure 18a, when the mass of the PMNES is set to 100, the green curve intersects the boundary of the SN bifurcation region, with the corresponding external excitation force thresholds being 1.5×10^3 and 11.5×10^3. These boundary values are consistent with the multistable regions illustrated in Figure 19a–c. Similarly, when the cubic nonlinear stiffness coefficient of the PMNES is set to 1×10^5, Figure 18b shows that the excitation force range of the SN bifurcation region spans from 2.7×10^3 to 15×10^3, which closely matches the multistable regions presented in Figure 19d–f. In Figure 18c, when the damping coefficient is set to 200, the SN bifurcation boundaries are located at 6.6×10^3 and 10×10^3, corresponding well with the multistable regions shown in Figure 19g–i. In summary, under a fixed external excitation circular frequency, the SN bifurcation boundaries of the system can be effectively predicted through the combination of PMNES parameters and excitation force amplitude. Furthermore, as shown in Figure 17, two stable solutions coexist in the multi-solution region, corresponding to lower and higher response amplitudes, respectively. These represent the lower and upper branches of the bifurcation curve, clearly reflecting the multistability phenomenon induced by SN bifurcations in nonlinear systems.

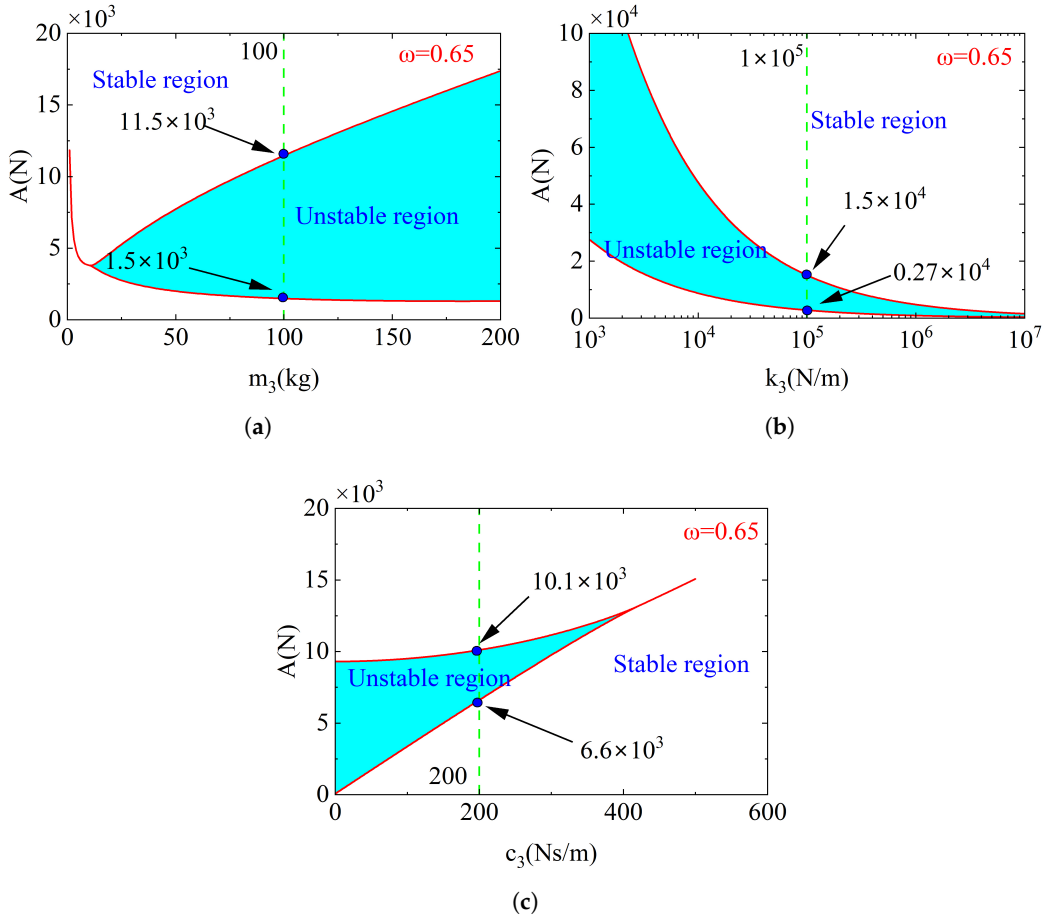


Figure 18. SN bifurcation diagram at external excitation circular frequency $\omega = 0.65$. (**a**) A–m_3 parameters plane. (**b**) A–k_3 parameters plane. (**c**) A–c_3 parameters plane.

3.3.2. Hopf Bifurcation at Specific Circular Frequency

Figure 20 illustrates the approximate solution regions associated with Hopf bifurcation. To accurately characterize the nonlinear dynamic behavior induced by Hopf bifurcation, the external excitation frequency was intentionally selected to be near the system's natural frequency (0.75). In this figure, the horizontal axis represents the mass of the NES, while the vertical axis denotes the amplitude of the external excitation force. The cyan-shaded region marks the Hopf bifurcation domain, within which unstable periodic solutions arise. Conversely, regions outside this domain correspond to dynamically stable responses. Under the specific configuration where the PMNES mass is fixed at 50 kg, the corresponding excitation force range that triggers bifurcation is clearly observed as $\left[1.25 \times 10^3, 2.4 \times 10^3\right]$. This behavior is further substantiated in Figure 21, which presents the amplitude responses of main structure 1, main structure 2, the PMNES, and the induced voltage. The horizontal axis in this figure again represents the magnitude of the external excitation force. The unstable dynamic response region, induced by Hopf bifurcation, corresponds directly to the bifurcation domain observed previously, with the excitation frequency held constant at 0.75. Notably, the boundaries of the Hopf bifurcation region are in exact agreement with the dynamic response threshold of the PMNES, validating the predictive accuracy of the bifurcation analysis.

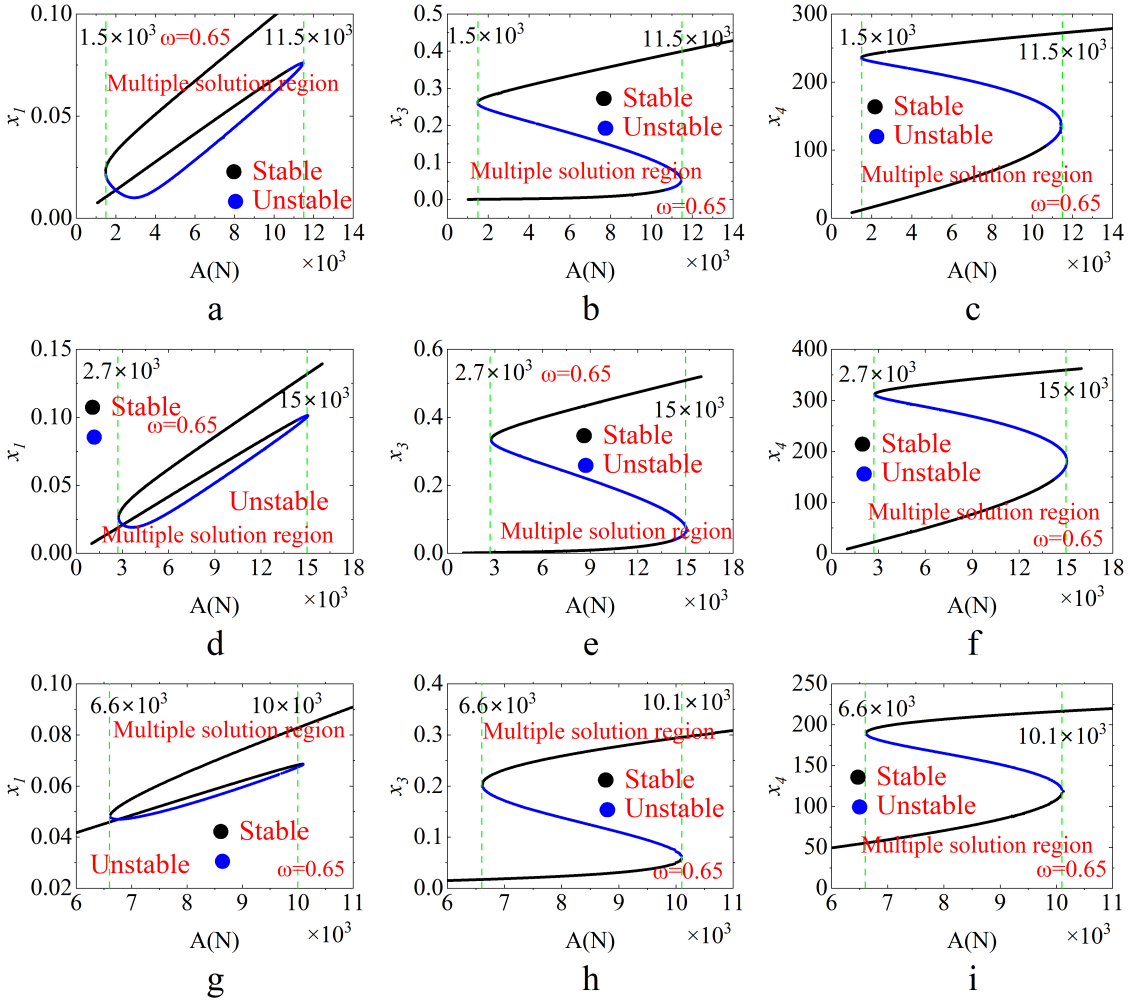


Figure 19. Bifurcation plots of system parameters with respect to main structure 1 magnitude, PMNES magnitude and voltage response. (**a**–**c**) A–m_3 parameters plane; (**d**–**f**) A–c_3 parameters plane; (**g**–**i**) A–k_3 parameters plane. (All amplitudes in the figure are dimensionless).

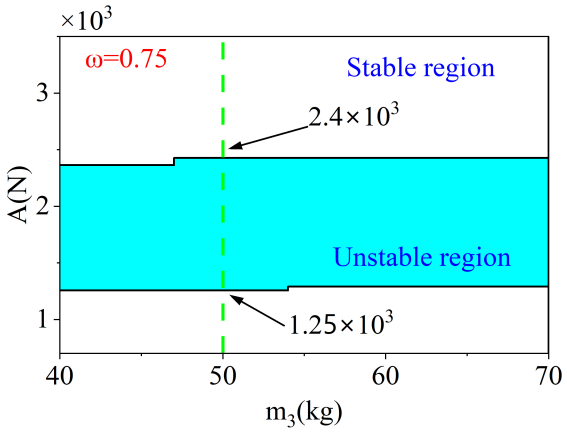


Figure 20. Hopf bifurcation diagram at external excitation circular frequency $\omega = 0.75$. $A - m_3$ parameters plane.

Figure 22 presents the bifurcation response of the numerical solution for the multi-degree-of-freedom (MDOF) PMNES system, serving as a validation of the approximate solution shown in Figure 21. The results indicate that the external excitation region for the numerical solution is $\left[1.25 \times 10^3, 2.4 \times 10^3\right]$, whereas that for the approximate solution is

$\left[2.4 \times 10^3, 1.25 \times 10^3\right]$. In studying the Hopf bifurcation regions of MDOF NES nonlinear energy sink systems, numerical solutions and the complex-averaging method are two primary approaches commonly employed to predict bifurcation boundaries. However, the sources of discrepancies between these methods are complex, particularly influenced by the inherent limitations of the complex-averaging method in MDOF systems. The complex-averaging method, a perturbation-based analytical approximation technique, simplifies the oscillatory behavior of nonlinear systems into low-order approximate solutions by introducing complex variables, making it suitable for analyzing the nascent amplitude and frequency of limit cycles. Nevertheless, its applicability is significantly constrained in MDOF systems, leading to deviations from the numerical solutions.

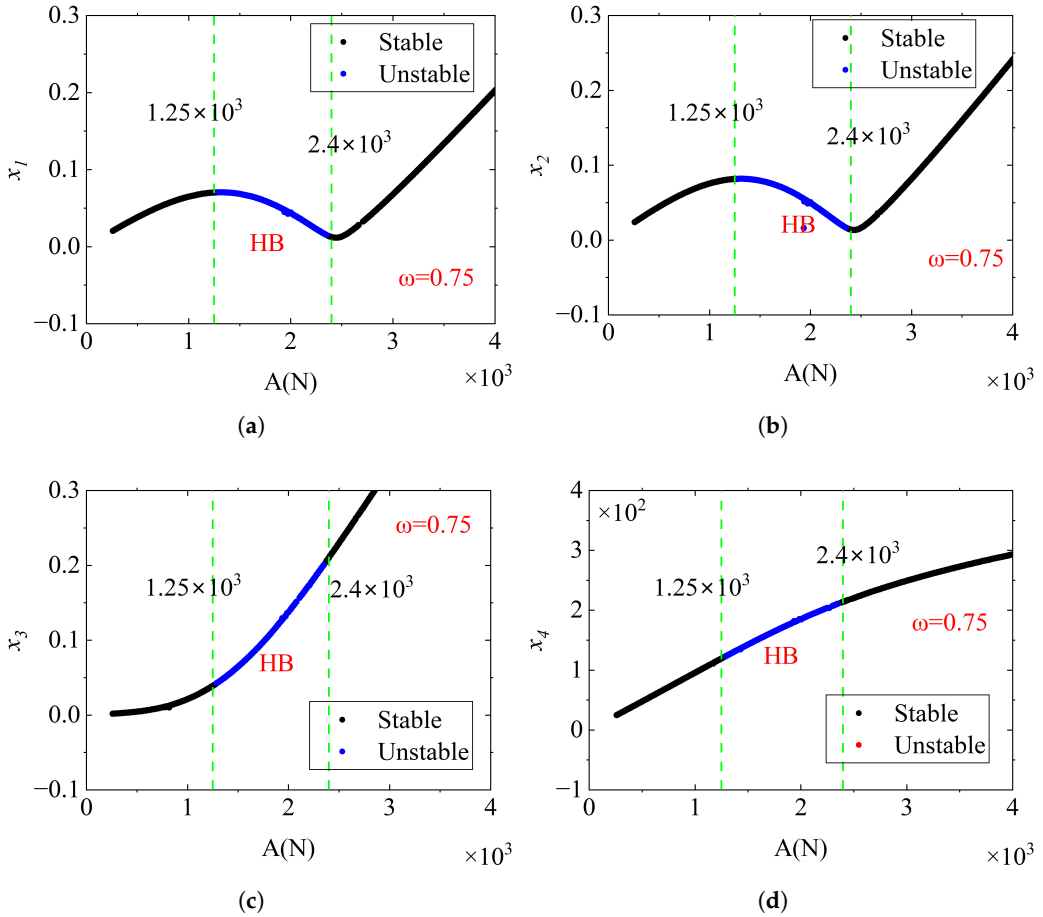


Figure 21. Hopf bifurcation under different external excitations. (**a**) Displacement amplitude of main structure 1. (**b**) Displacement amplitude of main structure 2. (**c**) Displacement amplitude of PMNES. (**d**) Displacement amplitude of voltage.

Figure 22 presents the bifurcation response derived from the numerical solution of the MDOF PMNES system, serving as a validation for the approximate solution previously shown in Figure 21. As indicated, the external excitation region associated with the numerical solution is $\left[1.25 \times 10^3, 2.4 \times 10^3\right]$, which is consistent with that predicted by the approximate solution, thereby confirming the reliability of the analytical method in capturing the bifurcation behavior.

PMNES exhibits broadband vibration suppression capability and high energy transfer efficiency, and has been widely applied in vibration control of various mechanical systems. In order to achieve vibration attenuation and energy harvesting functions of aerospace equipment, this study integrates piezoelectric elements into MNES to construct a PMNES

system. The research focuses on evaluating the output performance of PMNES through numerical analysis and approximate analytical methods. By applying Newton's second law and Kirchhoff's voltage law, a dimensionless electromechanical coupling governing equation is derived for a two-degree-of-freedom coupled PMNES system under harmonic excitation. Subsequently, the CX-A method is employed to obtain approximate analytical solutions, which are verified through comparison with numerical results obtained using the RK method. Based on the derived system equations, SN bifurcation points and cusp bifurcation points (codimension-2) are identified. An algorithm is introduced to determine the worst-case response amplitude across different excitation frequencies and to assess whether these bifurcation points correspond to HBs. This process allows for the delineation of bifurcation regions in the multi-DOF system, and the RK method is used to validate the bifurcation boundaries. The vibration suppression efficiency is quantitatively evaluated using generalized transmissibility, based on which efficiency zones are defined. By integrating the efficiency map with the bifurcation map, a comprehensive bifurcation-based vibration suppression diagram is constructed to characterize the system's mechanical behavior. The main conclusions of this study are as follows:

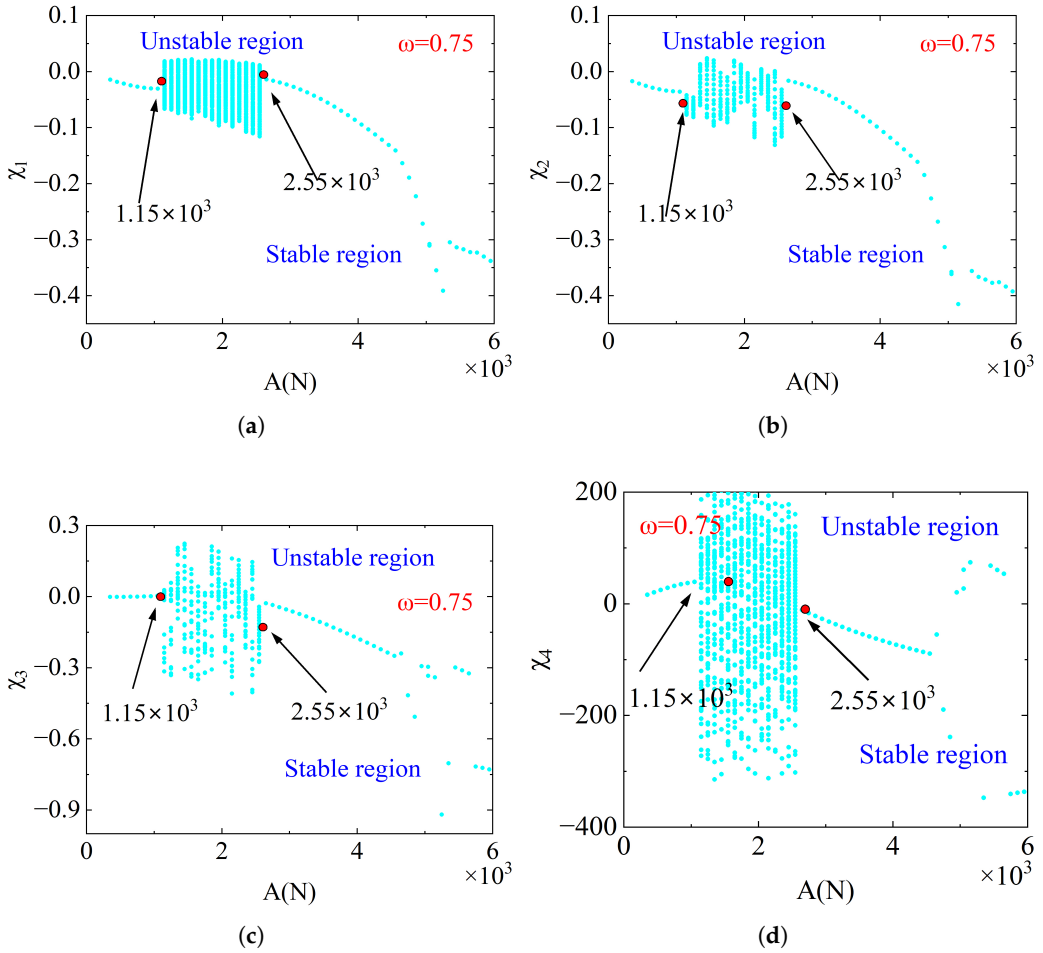


Figure 22. Bifurcation response under the Runge–Kutta numerical solution. (**a**) Displacement amplitude of main structure 1. (**b**) Displacement amplitude of main structure 2. (**c**) Displacement amplitude of PMNES. (**d**) Displacement amplitude of voltage.

It is emphasized that the effective operation of a nonlinear energy sink does not rely on a strictly exact 1:1:1 internal resonance condition. When the frequencies of the two dominant components of the primary structure and the NES oscillator are close to, but not exactly in, a 1:1:1 ratio, significant nonlinear energy transfer can still be achieved. By

appropriately selecting the equivalent mass, nonlinear stiffness, and damping parameters of the NES, the system can be tuned to operate within a near–1:1:1 internal resonance regime. With further parameter adjustments, the system response may enter an internal resonance region that is commonly associated with Hopf bifurcation behavior. This observation provides a physically reasonable basis for parameter tuning and practical implementation of PMNES in future engineering applications.

4. Conclusions

The core objective of this study is to elucidate how nonlinearity-induced bifurcation mechanisms influence vibration suppression and energy transfer processes in a multi-degree-of-freedom electromechanical system integrated with a PMNES. Motivated by aerospace applications, this study employs a generic two-degree-of-freedom low-order model to capture dominant low-frequency dynamics, rather than modeling a specific aerospace structure. Unlike a large body of existing studies that primarily emphasize performance enhancement or efficiency comparison, the present work focuses on the bifurcation structures and dynamic transition mechanisms introduced by nonlinear electromechanical coupling. Within this framework, the energy harvesting results are not treated as independent performance indicators. Instead, they are used to illustrate how electrical responses vary across different bifurcation regions, thereby highlighting the intrinsic link between nonlinear dynamic transitions and energy transfer behavior.

(1) Based on the proposed algorithm, a vibration suppression map is established to systematically correlate bifurcation characteristics with vibration attenuation performance. The map delineates multiple response regions according to bifurcation types and suppression efficiency, providing a clear characterization of the PMNES dynamic behavior within the adopted low-order dynamical modeling framework. Within this framework, the identified bifurcation boundaries and vibration suppression regions are applicable to flexible aerospace structures that exhibit similar dominant dynamic behavior.

(2) Under strong external excitation, an undesirable “frequency island” phenomenon may occur. As the excitation strength further increases, this island merges with the main response curve, leading to the emergence of a new vibration peak that shifts toward the lower frequency range. The appearance of this peak can be accurately predicted by identifying the cusp bifurcation points.

(3) In the HBVSR, due to the occurrence of HBs, PMNES achieves superior vibration suppression compared to the EVSR. In this region, PMNES exhibits a pronounced SMR effect, while the primary structure shows both effective vibration mitigation and high voltage output. In contrast, the AAR region is characterized by frequency islands and new peak phenomena, resulting in amplified vibration amplitudes. IVSR I and IVSR II are ineffective suppression zones with negligible vibration control capability.

(4) Reducing the mass ratio of PMNES or increasing its cubic stiffness lowers the external excitation threshold required for bifurcation. However, this may lead to amplitude amplification in the low-frequency range under small excitations, thereby compromising the broadband suppression performance.

(5) Increasing the damping coefficient of PMNES enhances the separation between SN and HB excitation thresholds, facilitating easier access to the HB suppression region. This also helps to avoid unfavorable phenomena such as frequency islands and low-frequency peak shifts.

Author Contributions: Conceptualization, M.Y., J.L. and Q.Y.; methodology, M.Y. and J.L.; software, M.Y.; validation, J.L. and Q.Y.; formal analysis, M.Y.; investigation, M.Y., J.L. and Q.Y.; resources, J.C., K.C., M.T. and T.L.; data curation, M.Y. and J.L.; writing—original draft preparation, M.Y.; writing—review and editing, J.L. and Q.Y.; visualization, M.Y.; supervision, Q.Y.; project administration, Q.Y.; funding acquisition, J.W. and X.B. All authors have read and agreed to the published version of the manuscript.

Funding: This research was supported by the National Natural Science Foundation of China (Grant No.: 52471354) and the Chongqing Graduate Research Innovation Project (Grant No.: CYS240797).

Data Availability Statement: The data presented in this study are available within the article. Further inquiries can be directed to the corresponding author.

Conflicts of Interest: The authors declare that they have no known competing financial interests or personal relationships that could have appeared to influence the work reported in this paper.

Appendix A

Appendix A.1

$$
\begin{aligned}
\Gamma_{11} &= \frac{\left((1+M_3)\,\lambda_2 + M_2^2\,(\lambda_1 + \lambda_2) + M_2(2\lambda_2 + M_3(\lambda_{\mathbf{1}} + \lambda_{\mathbf{2}}))\right)}{2M_2(1+M_2+M_3)} \\
\Gamma_{11j} &= -\frac{j\left(k_{21}\,(1+M_2)\,(1+M_2+M_3) + M_2^2\,(1-\omega^2) + M_2\left(-\omega^2 + M_3(1-\omega^2)\right)\right)}{2\omega M_2(1+M_2+M_3)} \\
\Gamma_{12} &= \frac{-(1+M_3)\,\lambda_3 + M_2(M_3\lambda_{\mathbf{1}} - \lambda_3)}{2M_2(1+M_2+M_3)}; \\
\Gamma_{12j} &= \frac{j\left(k_{p1} - k_{41}\right)(1+M_2+M_3) - jM_2M_3}{2\omega M_2(1+M_2+M_3)} \\
\Gamma_{13} &= \frac{\omega\lambda_{\mathbf{1}}}{2\omega(1+M_2+M_3)}; \\
\Gamma_{13j} &= \frac{-j}{2\omega(1+M_2+M_3)}; \\
\Gamma_{14j} &= \frac{3jk_{31}}{8M_2\omega^3}
\end{aligned}
\tag{A1}
$$

$$
\begin{aligned}
\Gamma_{21} &= \frac{-\omega\lambda_2}{2\omega M_2}; \\
\Gamma_{21j} &= \frac{jk_{21}}{2\omega M_2} \\
\Gamma_{22} &= \frac{M_2\lambda_3 + M_3\lambda_3}{2M_2M_3}; \\
\Gamma_{22j} &= -\frac{j\left(\left(-k_{41} + k_{p1}\right)(M_2+M_3) - \omega^2 M_2M_3\right)}{2\omega M_2M_3} \\
\Gamma_{23j} &= -\frac{3jk_{31}(M_2+M_3)}{8\omega^3 M_2M_3}
\end{aligned}
\tag{A2}
$$

$$\begin{aligned}
\Gamma_{31} &= \frac{\omega\lambda_1(M_2+M_3)}{2\omega(1+M_2+M_3)};\\
\Gamma_{31j} &= \frac{-j(M_2+M_3)}{2\omega(1+M_2+M_3)}\\
\Gamma_{32} &= \frac{M_3\omega\lambda_1}{2\omega(1+M_2+M_3)};\\
\Gamma_{32j} &= \frac{-jM_3}{2\omega(1+M_2+M_3)}\\
\Gamma_{33} &= \frac{\omega\lambda_1}{2\omega(1+M_2+M_3)};\\
\Gamma_{33j} &= \frac{j\left(-1+\omega^2(M_2+M_3)\right)}{2\omega(1+M_2+M_3)}
\end{aligned} \tag{A3}$$

Appendix A.2

$$\Psi_0 = \frac{\Psi_{01}}{\Psi_{02}}; \Psi_1 = \frac{\Psi_{11}}{\Psi_{12}}; \Psi_2 = \frac{\Psi_{21}}{\Psi_{22}}; \Psi_3 = \frac{\Psi_{31}}{\Psi_{22}}; \tag{A4}$$

$$\Psi_{01} = A_1^2(M_2+M_3+1)^2\omega^4\left(\lambda_2^2\omega^2+k_{21}^2\right) \tag{A5}$$

$$\begin{aligned}
\Psi_{02} &= 4(-2\omega^2k_{21}M_2(1+M_2)(1+M_2+M_3)(1-2\omega^2+\omega^4+\omega^2(-1+\omega^2)M_2\\
&+\omega^2(-1+\omega^2)M_3+\omega^2\lambda_1^2)+k_{21}^2(1+M_2)^2(1-2\omega^2+\omega^4+\omega^4M_2^2+2\omega^2(-1+\omega^2)M_3\\
&+\omega^4M_3^2+2\omega^2M_2(-1+\omega^2+\omega^2M_3)+\omega^2\lambda_1^2)+\omega^2(((-1+\omega^2)^2+2\omega^2(-1+\omega^2)M_3\\
&+\omega^4M_3^2+\omega^2\lambda_1^2)\lambda_2^2+M_2^4(\omega^2(-1+\omega^2)^2+\omega^4\lambda_1^2+2\omega^4\lambda_1\lambda_2+\omega^4\lambda_2^2)+2M_2\lambda_2((1-3\omega^2\\
&+2\omega^4+\omega^2\lambda_1^2)\lambda_2+\omega^4M_3^2(\lambda_1+\lambda_2)+M_3(\omega^4\lambda_1+\omega^2(-2+3\omega^2)\lambda_2))+2\omega^2M_2^3(1-2\omega^2\\
&+\omega^4+\omega^2\lambda_1^2+2\omega^2\lambda_1\lambda_2-\lambda_2^2+2\omega^2\lambda_2^2+M_3((-1+\omega^2)^2+\omega^2\lambda_1^2+2\omega^2\lambda_1\lambda_2+\omega^2\lambda_2^2))\\
&+M_2^2(\omega^2-2\omega^4+\omega^6+\omega^4\lambda_1^2+2\omega^4\lambda_1\lambda_2+\lambda_2^2-6\omega^2\lambda_2^2+6\omega^4\lambda_2^2+\omega^2\lambda_1^2\lambda_2^2+M_3^2(\omega^2(-1\\
&+\omega^2)^2+\omega^4\lambda_1^2+2\omega^4\lambda_1\lambda_2+\omega^4\lambda_2^2)+2\omega^2M_3((-1+\omega^2)^2+\omega^2\lambda_1^2+3\omega^2\lambda_1\lambda_2+(-1+3\omega^2)\lambda_2^2))))
\end{aligned} \tag{A6}$$

$$\Psi_{11} = (M_2+M_3+1)^2(\Psi_{111}+\Psi_{112}+\Psi_{113}+\Psi_{114}) \tag{A7}$$

$$\begin{aligned}
\Psi_{111} &= -2\omega^4k_{p1}(M_2^2\omega^2((\lambda_1+\lambda_2)^2\omega^2+\omega^4-2\omega^2+1)(M_3(\mathrm{Cpp}^2\omega^2R_{n1}^2+1)-\mathrm{Cpp}\theta_m\theta_nR_{n1}^2)\\
&+M_2\omega^2(M_3^2((\lambda_1+\lambda_2)^2\omega^2+\omega^4-2\omega^2+1)(\mathrm{Cpp}^2\omega^2R_{n1}^2+1)+2M_3(\mathrm{Cpp}R_{n1}^2(\mathrm{Cpp}\lambda_2^2\omega^2(\omega^2-1)\\
&-((\lambda_1+\lambda_2)^2\omega^2+\omega^4-2\omega^2+1)\theta_m\theta_n)+\lambda_2^2(\omega^2-1))-2\mathrm{Cpp}\lambda_2^2(\omega^2-1)\theta_m\theta_nR_{n1}^2)+\lambda_2^2M_3\\
&(\mathrm{Cpp}\omega^2R_{n1}^2(\mathrm{Cpp}(\lambda_1^2\omega^2+(\omega^2-1)^2)-2(\omega^2-1)\theta_m\theta_n)+\lambda_1^2\omega^2+(\omega^2-1)^2)+M_3^2\omega^2(\mathrm{Cpp}R_{n1}^2(\mathrm{Cpp}\\
&\lambda_2^2\omega^2(\omega^2-1)-((\lambda_1+\lambda_2)^2\omega^2+\omega^4-2\omega^2+1)\theta_m\theta_n)+\lambda_2^2(\omega^2-1))-\mathrm{Cpp}\lambda_2^2(\lambda_1^2\omega^2+(\omega^2-1)^2)\theta_m\\
&\theta_nR_{n1}^2)+\omega^2k_{p1}^2(2\lambda_1\lambda_2(M_2+M_3)^2\omega^4+(M_2+M_3)^2\omega^2(\lambda_1^2\omega^2+(\omega^2-1)^2)+\lambda_2^2(\lambda_1^2\omega^2+((M_2+M_3)\\
&\omega^2+\omega^2-1)^2))(\mathrm{Cpp}^2\omega^2R_{n1}^2+1)+M_2^2\omega^6((\lambda_1+\lambda_2)^2\omega^2+\omega^4-2\omega^2+1)(R_{n1}^2(\mathrm{Cpp}^2\lambda_3^2\omega^2+\theta_m^2\theta_n^2)\\
&+M_3^2(\mathrm{Cpp}^2\omega^4R_{n1}^2+\omega^2)-2\mathrm{Cpp}M_3\omega^2\theta_m\theta_nR_{n1}^2+\lambda_3^2-2\lambda_3\theta_m\theta_nR_{n1})+\lambda_2^2\omega^4(\lambda_1^2\omega^2+(\omega^2-1)^2)\\
&(R_{n1}^2(\mathrm{Cpp}^2\lambda_3^2\omega^2+\theta_m^2\theta_n^2)+\lambda_3^2-2\lambda_3\theta_m\theta_nR_{n1}))
\end{aligned} \tag{A8}$$

$$\begin{aligned}\Psi_{112} = {} & 2\lambda_2^2 M_3\omega^6(R_{n1}^2(\mathrm{Cpp}^2\lambda_3^2\omega^2(\omega^2-1)+\theta_m\theta_n((\omega^2-1)\theta_m\theta_n-\mathrm{Cpp}(\lambda_1^2\omega^2+(\omega^2-1)^2)))\\ & +\lambda_3^2(\omega^2-1)-2\lambda_3(\omega^2-1)\theta_m\theta_n R_{n1})+2M_2\omega^6(M_3(\lambda_3^2((\lambda_1+\lambda_2)^2\omega^2+\omega^4-2\omega^2+1)(\mathrm{Cpp}^2\omega^2R_{n1}^2\\ & +1)+\theta_m\theta_n R_{n1}^2(((\lambda_1+\lambda_2)^2\omega^2+\omega^4-2\omega^2+1)\theta_m\theta_n-2\mathrm{Cpp}\lambda_2^2\omega^2(\omega^2-1))-2\lambda_3((\lambda_1+\lambda_2)^2\omega^2\\ & +\omega^4-2\omega^2+1)\theta_m\theta_n R_{n1})+\lambda_2^2(\omega^2-1)(R_{n1}^2(\mathrm{Cpp}^2\lambda_3^2\omega^2+\theta_m^2\theta_n^2)+\lambda_3^2-2\lambda_3\theta_m\theta_n R_{n1})+M_3^2\omega^2(\mathrm{Cpp}\\ & R_{n1}^2(\mathrm{Cpp}\lambda_2^2\omega^2(\omega^2-1)-((\lambda_1+\lambda_2)^2\omega^2+\omega^4-2\omega^2+1)\theta_m\theta_n)+\lambda_2^2(\omega^2-1)))+M_3^2\omega^6(R_{n1}^2(\mathrm{Cpp}^2\omega^2\\ & (\lambda_3^2(\lambda_1^2\omega^2+(\omega^2-1)^2)+\lambda_2^2((\lambda_1+\lambda_3)^2\omega^2+\omega^4-2\omega^2+1)+2\lambda_3\lambda_2(\lambda_1(\lambda_1+\lambda_3)\omega^2+\omega^4-2\omega^2+1))\\ & -2\mathrm{Cpp}\lambda_2^2(\omega^2-1)\omega^2\theta_m\theta_n+((\lambda_1+\lambda_2)^2\omega^2+\omega^4-2\omega^2+1)\theta_m^2\theta_n^2)+\lambda_3^2(\lambda_1^2\omega^2+(\omega^2-1)^2)+2\lambda_2\lambda_3\\ & (\lambda_1(\lambda_1+\lambda_3)\omega^2+\omega^4-2\omega^2+1)+\lambda_2^2((\lambda_1+\lambda_3)^2\omega^2+\omega^4-2\omega^2+1)-2(\lambda_3\omega^2((\lambda_1+\lambda_2)^2+\omega^2-2)\\ & +\lambda_2(\lambda_1(\lambda_1+\lambda_2)\omega^2+\omega^4-2\omega^2+1)+\lambda_3)\theta_m\theta_n R_{n1})\end{aligned} \tag{A9}$$

$$\begin{aligned}\Psi_{113} = {} & -2k_{21}-k_{p1}(2\omega^2(\omega^2-1)(M_3(\mathrm{Cpp}^2\omega^2R_{n1}^2+1)-\mathrm{Cpp}R_{n1}^2\theta_m\theta_n)M_2^2+2(\omega^2(M_3(\mathrm{Cpp}^2\omega^2R_{n1}^2\\ & +1)-\mathrm{Cpp}R_{n1}^2\theta_m\theta_n)\lambda_1^2+(\omega^2-1)(M_3(M_3\omega^2+\omega^2-1)(\mathrm{Cpp}^2\omega^2R_{n1}^2+1)-\mathrm{Cpp}(2M_3\omega^2+\omega^2-1)\\ & R_{n1}^2\theta_m\theta_n))M_2+M_3(M_3(\omega^4+(\mathrm{Cpp}(\mathrm{Cpp}\omega^2\lambda_1^2+(\omega^2-1)(\mathrm{Cpp}(\omega^2-1)-2\theta_m\theta_n))R_{n1}^2+\lambda_1^2)\omega^2-2\omega^2\\ & +1)-2\mathrm{Cpp}R_{n1}^2\theta_m\theta_n((\omega^2-1)^2+\omega^2\lambda_1^2)))\omega^4+(\omega^2(\omega^2-1)((\mathrm{Cpp}^2R_{n1}^2\omega^4+\omega^2)M_3^2-2\mathrm{Cpp}\omega^2R_{n1}^2\\ & \theta_m\theta_n M_3+\lambda_3^2-2R_{n1}\theta_m\theta_n\lambda_3+R_{n1}^2(\theta_m^2\theta_n^2+\mathrm{Cpp}^2\omega^2\lambda_3^2))M_2^2+(M_3^2((\omega^2-1)^2+\omega^2\lambda_1^2+\mathrm{Cpp}\omega^2\\ & R_{n1}^2(\mathrm{Cpp}\omega^2\lambda_1^2+(\omega^2-1)(\mathrm{Cpp}(\omega^2-1)-2\theta_m\theta_n)))\omega^2+2M_3(-2(\omega^2-1)\theta_m\theta_n\lambda_3R_{n1}+(\omega^2-1)\\ & (\mathrm{Cpp}^2\omega^2R_{n1}^2+1)\lambda_3^2-R_{n1}^2\theta_m\theta_n(\mathrm{Cpp}((\omega^2-1)^2+\omega^2\lambda_1^2)-(\omega^2-1)\theta_m\theta_n))\omega^2+((\omega^2-1)^2+\omega^2\lambda_1^2)\\ & ((\theta_m^2\theta_n^2+\mathrm{Cpp}^2\omega^2\lambda_3^2)R_{n1}^2-2\theta_m\theta_n\lambda_3R_{n1}+\lambda_3^2))M_2+M_3(M_3(-2(\omega^2-1)\theta_m\theta_n\lambda_3R_{n1}+(\omega^2-1)\\ & (\mathrm{Cpp}^2\omega^2R_{n1}^2+1)\lambda_3^2-R_{n1}^2\theta_m\theta_n(\mathrm{Cpp}((\omega^2-1)^2+\omega^2\lambda_1^2)-(\omega^2-1)\theta_m\theta_n))\omega^2+((\omega^2-1)^2+\omega^2\lambda_1^2)\\ & ((\theta_m^2\theta_n^2+\mathrm{Cpp}^2\omega^2\lambda_3^2)R_{n1}^2-2\theta_m\theta_n\lambda_3R_{n1}+\lambda_3^2)))\omega^4+k_{p1}^2(M_2+M_3)(\mathrm{Cpp}^2\omega^2R_{n1}^2+1)(\omega^2\lambda_1^2+(\omega^2-1)\\ & ((M_2+M_3)\omega^2+\omega^2-1))\omega^2\end{aligned} \tag{A10}$$

$$\begin{aligned}\Psi_{114} = {} & k_{21}^2(-2\omega^2k_{p1}(M_3((M_2\omega^2+\omega^2-1)((M_2\omega^2+\omega^2-1)(\mathrm{Cpp}^2\omega^2R_{n1}^2+1)-2\mathrm{Cpp}\omega^2\theta_m\theta_nR_{n1}^2)\\ & +\lambda_1^2\omega^2(\mathrm{Cpp}^2\omega^2R_{n1}^2+1))+M_3^2\omega^2((M_2\omega^2+\omega^2-1)(\mathrm{Cpp}^2\omega^2R_{n1}^2+1)-\mathrm{Cpp}\omega^2\theta_m\theta_nR_{n1}^2)+\mathrm{Cpp}\theta_m\\ & \theta_nR_{n1}^2(-\lambda_1^2\omega^2-(M_2\omega^2+\omega^2-1)^2))+k_{p1}^2(\lambda_1^2\omega^2+((M_2+M_3)\omega^2+\omega^2-1)^2)(\mathrm{Cpp}^2\omega^2R_{n1}^2+1)\\ & +\omega^2(2M_3\omega^2(\lambda_3^2(M_2\omega^2+\omega^2-1)(\mathrm{Cpp}^2\omega^2R_{n1}^2+1)+\theta_m\theta_nR_{n1}^2((M_2\omega^2+\omega^2-1)(\theta_m\theta_n-\mathrm{Cpp}\\ & (M_2\omega^2+\omega^2-1))-\mathrm{Cpp}\lambda_1^2\omega^2)-2\lambda_3\theta_m(M_2\omega^2+\omega^2-1)\theta_nR_{n1})+(\lambda_1^2\omega^2+(M_2\omega^2+\omega^2-1)^2)\\ & (R_{n1}^2(\mathrm{Cpp}^2\lambda_3^2\omega^2+\theta_m^2\theta_n^2)+\lambda_3^2-2\lambda_3\theta_m\theta_nR_{n1})+M_3^2(\omega^4(R_{n1}^2(\mathrm{Cpp}^2((\lambda_1+\lambda_3)^2\omega^2+\omega^4-2\omega^2+1)\\ & -2\mathrm{Cpp}(\omega^2-1)\theta_m\theta_n+\theta_m^2\theta_n^2)+M_2^2(\mathrm{Cpp}^2\omega^4R_{n1}^2+\omega^2)+2M_2(\mathrm{Cpp}\omega^2R_{n1}^2(\mathrm{Cpp}(\omega^2-1)\\ & -\theta_m\theta_n)+\omega^2-1)+(\lambda_1+\lambda_3)^2-2(\lambda_1+\lambda_3)\theta_m\theta_nR_{n1})+\omega^6-2\omega^4+\omega^2))))\end{aligned} \tag{A11}$$

$$\begin{aligned}\Psi_{12} = {} & 4M_3^2\omega^2(\mathrm{Cpp}^2\omega^2R_{n1}^2+1)(-2k_{21}M_2(M_2+1)(M_2+M_3+1)\omega^2(\omega^2(\lambda_1^2+(M_2+M_3)(\omega^2-1))\\ & +(\omega^2-1)^2)+k_{21}^2(M_2+1)^2(\lambda_1^2\omega^2+((M_2+M_3)\omega^2+\omega^2-1)^2)+2\lambda_1\lambda_2M_2(M_2+1)\\ & (M_2+M_3)(M_2+M_3+1)\omega^6+\lambda_2^2(M_2+1)^2\omega^2(\lambda_1^2\omega^2+((M_2+M_3)\omega^2+\omega^2-1)^2)\\ & +M_2^2(M_2+M_3+1)^2\omega^4(\lambda_1^2\omega^2+(\omega^2-1)^2))\end{aligned} \tag{A12}$$

$$\Psi_{21} = 3k_{31}(M_2+M_3+1)^2(\Psi_{211}+\Psi_{212}) \tag{A13}$$

$$\begin{aligned}\Psi_{211} = {} & k_{21}(\omega^4(2M_2(M_3^2\omega^2(\omega^2-1)(\mathrm{Cpp}^2\omega^2R_{n1}^2+1)+M_3(\mathrm{Cpp}\omega^2R_{n1}^2(\mathrm{Cpp}(\lambda_1^2\omega^2+(\omega^2-1)^2)\\ & -2(\omega^2-1)\theta_m\theta_n)+\lambda_1^2\omega^2+(\omega^2-1)^2)-\mathrm{Cpp}(\lambda_1^2\omega^2+(\omega^2-1)^2)\theta_m\theta_nR_{n1}^2)+2M_2^2\omega^2(\omega^2-1)\\ & (M_3(\mathrm{Cpp}^2\omega^2R_{n1}^2+1)-\mathrm{Cpp}\theta_m\theta_nR_{n1}^2)+M_3(M_3(\mathrm{Cpp}\omega^2R_{n1}^2(\mathrm{Cpp}(\lambda_1^2\omega^2+(\omega^2-1)^2)-2(\omega^2-1)\\ & \theta_m\theta_n)+\lambda_1^2\omega^2+(\omega^2-1)^2)-2\mathrm{Cpp}(\lambda_1^2\omega^2+(\omega^2-1)^2)\theta_m\theta_nR_{n1}^2))-2(M_2+M_3)\omega^2k_{p1}(\lambda_1^2\omega^2\\ & +M_2(\omega^2-1)\omega^2+M_3(\omega^2-1)\omega^2+\omega^4-2\omega^2+1)(\mathrm{Cpp}^2\omega^2R_{n1}^2+1))+k_{21}^2(k_{p1}(\lambda_1^2\omega^2+M_2^2\omega^4\\ & +M_3^2\omega^4+2M_3(\omega^2-1)\omega^2+2M_2\omega^2(M_3\omega^2+\omega^2-1)+\omega^4-2\omega^2+1)(\mathrm{Cpp}^2\omega^2R_{n1}^2+1)-\omega^2\\ & (M_3(M_2^2(\mathrm{Cpp}^2\omega^6R_{n1}^2+\omega^4)+2M_2\omega^2(\mathrm{Cpp}\omega^2R_{n1}^2(\mathrm{Cpp}(\omega^2-1)-\theta_m\theta_n)+\omega^2-1)+\mathrm{Cpp}\omega^2R_{n1}^2\\ & (\mathrm{Cpp}(\lambda_1^2\omega^2+(\omega^2-1)^2)-2(\omega^2-1)\theta_m\theta_n)+\lambda_1^2\omega^2+\omega^4-2\omega^2+1)+M_3^2\omega^2(M_2(\mathrm{Cpp}^2\omega^4R_{n1}^2\\ & +\omega^2)+\mathrm{Cpp}\omega^2R_{n1}^2(\mathrm{Cpp}(\omega^2-1)-\theta_m\theta_n)+\omega^2-1)-\mathrm{Cpp}\theta_m\theta_nR_{n1}^2(\lambda_1^2\omega^2+M_2^2\omega^4+\\ & 2M_2(\omega^2-1)\omega^2+(\omega^2-1)^2))))\end{aligned} \tag{A14}$$

$$\begin{aligned}\Psi_{212} = {} & \omega^2k_{p1}(\lambda_2^2(\lambda_1^2\omega^2+(\omega^2-1)^2)+2\lambda_2^2M_3(\omega^2-1)\omega^2+2M_2\omega^2(\lambda_2^2(\omega^2-1)+M_3(\lambda_1^2\omega^2\\ & +\lambda_2^2\omega^2+2\lambda_1\lambda_2\omega^2+(\omega^2-1)^2))+M_2^2(\lambda_1^2\omega^4+\lambda_2^2\omega^4+2\lambda_1\lambda_2\omega^4+(\omega^2-1)^2\omega^2)+M_3^2(\lambda_1^2\omega^4\\ & +\lambda_2^2\omega^4+2\lambda_1\lambda_2\omega^4+(\omega^2-1)^2\omega^2))(\mathrm{Cpp}^2\omega^2R_{n1}^2+1)-\omega^4(M_2^2\omega^2(\lambda_1^2\omega^2+\lambda_2^2\omega^2+2\lambda_1\lambda_2\omega^2\\ & +(\omega^2-1)^2)(M_3(\mathrm{Cpp}^2\omega^2R_{n1}^2+1)-\mathrm{Cpp}\theta_m\theta_nR_{n1}^2)+M_2\omega^2(M_3^2(\lambda_1^2\omega^2+\lambda_2^2\omega^2+2\lambda_1\lambda_2\omega^2\\ & +(\omega^2-1)^2)(\mathrm{Cpp}^2\omega^2R_{n1}^2+1)+2M_3(\mathrm{Cpp}R_{n1}^2(\mathrm{Cpp}\lambda_2^2\omega^2(\omega^2-1)-(\lambda_1^2\omega^2+\lambda_2^2\omega^2+2\lambda_1\lambda_2\omega^2\\ & +(\omega^2-1)^2)\theta_m\theta_n)+\lambda_2^2(\omega^2-1))-2\mathrm{Cpp}\lambda_2^2(\omega^2-1)\theta_m\theta_nR_{n1}^2)+M_3^2\omega^2(\mathrm{Cpp}R_{n1}^2(\mathrm{Cpp}\lambda_2^2\omega^2(\omega^2\\ & -1)-(\lambda_1^2\omega^2+\lambda_2^2\omega^2+2\lambda_1\lambda_2\omega^2+(\omega^2-1)^2)\theta_m\theta_n)+\lambda_2^2(\omega^2-1))+\lambda_2^2M_3(\mathrm{Cpp}\omega^2R_{n1}^2(\mathrm{Cpp}\\ & (\lambda_1^2\omega^2+(\omega^2-1)^2)-2(\omega^2-1)\theta_m\theta_n)+\lambda_1^2\omega^2+(\omega^2-1)^2)-\mathrm{Cpp}\lambda_2^2(\lambda_1^2\omega^2+(\omega^2-1)^2)\theta_m\theta_nR_{n1}^2)\end{aligned} \tag{A15}$$

$$\begin{aligned}\Psi_{22} = {} & 8M_3^2\omega^4(\mathrm{Cpp}^2\omega^2R_{n1}^2+1)(-2k_{21}M_2(M_2+1)(M_2+M_3+1)\omega^2(\lambda_1^2\omega^2+M_2(\omega^2-1)\omega^2\\ & +M_3(\omega^2-1)\omega^2+\omega^4-2\omega^2+1)+k_{21}^2(M_2+1)^2(\lambda_1^2\omega^2+M_2^2\omega^4+M_3^2\omega^4+2M_3(\omega^2-1)\omega^2+\\ & 2M_2\omega^2(M_3\omega^2+\omega^2-1)+\omega^4-2\omega^2+1)+\omega^2(M_2^4(\lambda_1^2\omega^4+\lambda_2^2\omega^4+2\lambda_1\lambda_2\omega^4+(\omega^2-1)^2\omega^2)\\ & +2M_2^3\omega^2(\lambda_1^2\omega^2+2\lambda_2^2\omega^2+2\lambda_1\lambda_2\omega^2-\lambda_2^2+M_3(\lambda_1^2\omega^2+\lambda_2^2\omega^2+2\lambda_1\lambda_2\omega^2+(\omega^2-1)^2)+\omega^4\\ & -2\omega^2+1)+2\lambda_2M_2(\lambda_2(\lambda_1^2\omega^2+2\omega^4-3\omega^2+1)+(\lambda_1+\lambda_2)M_3^2\omega^4+M_3(\lambda_1\omega^4+\lambda_2(3\omega^2-2)\omega^2))\\ & +\lambda_2^2(\lambda_1^2\omega^2+M_3^2\omega^4+2M_3(\omega^2-1)\omega^2+(\omega^2-1)^2)+M_2^2(\lambda_1^2\omega^4+6\lambda_2^2\omega^4+2\lambda_1\lambda_2\omega^4+\lambda_1^2\lambda_2^2\omega^2\\ & -6\lambda_2^2\omega^2+\lambda_2^2+2M_3\omega^2(\lambda_1^2\omega^2+3\lambda_1\lambda_2\omega^2+\lambda_2^2(3\omega^2-1)+(\omega^2-1)^2)+M_3^2(\lambda_1^2\omega^4+\lambda_2^2\omega^4\\ & +2\lambda_1\lambda_2\omega^4+(\omega^2-1)^2\omega^2)+\omega^6-2\omega^4+\omega^2)))\end{aligned} \tag{A16}$$

$$\begin{aligned}\Psi_{31} = {} & 9k_{31}^2(M_2+M_3+1)^2(-2k_{21}(M_2+M_3)\omega^2(\lambda_1^2\omega^2+M_2(\omega^2-1)\omega^2+M_3(\omega^2-1)\omega^2+\omega^4\\ & -2\omega^2+1)+k_{21}^2(\lambda_1^2\omega^2+M_2^2\omega^4+M_3^2\omega^4+2M_3(\omega^2-1)\omega^2+2M_2\omega^2(M_3\omega^2+\omega^2-1)+\omega^4\\ & -2\omega^2+1)+\omega^2(\lambda_2^2(\lambda_1^2\omega^2+(\omega^2-1)^2)+2\lambda_2^2M_3(\omega^2-1)\omega^2+2M_2\omega^2(\lambda_2^2(\omega^2-1)+M_3(\lambda_1^2\omega^2\\ & +\lambda_2^2\omega^2+2\lambda_1\lambda_2\omega^2+(\omega^2-1)^2))+M_2^2(\lambda_1^2\omega^4+\lambda_2^2\omega^4+2\lambda_1\lambda_2\omega^4+(\omega^2-1)^2\omega^2)\\ & +M_3^2(\lambda_1^2\omega^4+\lambda_2^2\omega^4+2\lambda_1\lambda_2\omega^4+(\omega^2-1)^2\omega^2)))\end{aligned} \tag{A17}$$

$$\begin{aligned}\Psi_{32} = {} & 64M_3^2\omega^6(-2k_{21}M_2(M_2+1)(M_2+M_3+1)\omega^2(\lambda_1^2\omega^2+M_2(\omega^2-1)\omega^2+M_3(\omega^2-1)\omega^2\\ & +\omega^4-2\omega^2+1)+k_{21}^2(M_2+1)^2(\lambda_1^2\omega^2+M_2^2\omega^4+M_3^2\omega^4+2M_3(\omega^2-1)\omega^2+2M_2\omega^2(M_3\omega^2\\ & +\omega^2-1)+\omega^4-2\omega^2+1)+\omega^2(M_2^4(\lambda_1^2\omega^4+\lambda_2^2\omega^4+2\lambda_1\lambda_2\omega^4+(\omega^2-1)^2\omega^2)+2M_2^3\omega^2(\lambda_1^2\omega^2\\ & +2\lambda_2^2\omega^2+2\lambda_1\lambda_2\omega^2-\lambda_2^2+M_3(\lambda_1^2\omega^2+\lambda_2^2\omega^2+2\lambda_1\lambda_2\omega^2+(\omega^2-1)^2)+\omega^4-2\omega^2+1)\\ & +2\lambda_2M_2(\lambda_2(\lambda_1^2\omega^2+2\omega^4-3\omega^2+1)+(\lambda_1+\lambda_2)M_3^2\omega^4+M_3(\lambda_1\omega^4+\lambda_2(3\omega^2-2)\omega^2))\\ & +\lambda_2^2(\lambda_1^2\omega^2+M_3^2\omega^4+2M_3(\omega^2-1)\omega^2+(\omega^2-1)^2)+M_2^2(\lambda_1^2\omega^4+6\lambda_2^2\omega^4+2\lambda_1\lambda_2\omega^4+\lambda_1^2\lambda_2^2\omega^2\\ & -6\lambda_2^2\omega^2+\lambda_2^2+2M_3\omega^2(\lambda_1^2\omega^2+3\lambda_1\lambda_2\omega^2+\lambda_2^2(3\omega^2-1)\\ & +(\omega^2-1)^2)+M_3^2(\lambda_1^2\omega^4+\lambda_2^2\omega^4+2\lambda_1\lambda_2\omega^4+(\omega^2-1)^2\omega^2)+\omega^6-2\omega^4+\omega^2)))\end{aligned} \tag{A18}$$

References

1. Dou, J.; Yao, H.; Li, H. A track nonlinear energy sink with restricted motion for rotor systems. *Int. J. Mech. Sci.* **2024**, *185*, 115144. [CrossRef]
2. Geng, X.F.; Ding, H.; Ji, J.C.; Chen, L.Q. A state-of-the-art review on the dynamic design of nonlinear energy sinks. *Eng. Struct.* **2024**, *313*, 118228. [CrossRef]
3. Lee, Y.S.; Vakakis, A.F.; Bergman, L.A. Suppression aeroelastic instability using broadband passive targeted energy transfers, part 1: Theory. *AIAA J.* **2007**, *45*, 693711. [CrossRef]
4. Zhou, S.Y.; Claire, J.M.; Chesne, S. Influence of inerters on the vibration control effect of series double tuned mass dampers: Two layouts and analytical study. *Struct. Control Health Monit.* **2019**, *26*, 02435315. [CrossRef]
5. Liu, C.; Jing, X.; Daley, S.; Li, F. Recent advances in micro-vibration isolation. *Mech. Syst. Signal Process.* **2015**, *56–57*, 55–80. [CrossRef]
6. Wang, T.; Ding, Q. Targeted energy transfer analysis of a nonlinear oscillator coupled with bistable nonlinear energy sink based on nonlinear normal modes. *J. Sound Vib.* **2023**, *556*, 117727. [CrossRef]
7. Dekemele, K.; Van Torre, P.; Loccufier, M. Design, construction and experimental performance of a nonlinear energy sink in mitigating multi-modal vibrations. *J. Sound Vib.* **2020**, *473*, 115243. [CrossRef]
8. Fu, J.; Wan, S.; Zhou, P. Effect of magnetic-spring bistable nonlinear energy sink on vibration and damage reduction of concrete double-column piers: Experimental and numerical analysis. *Eng. Struct.* **2024**, *271*, 109305.
9. Zang, J.; Zhang, Y.W.; Ding, H.; Chen, L.Q. The evaluation of a nonlinear energy sink absorber based on the transmissibility. *Mech. Syst. Signal Process.* **2019**, *125*, 99122. [CrossRef]
10. Yang, K.; Zhang, Y.W.; Ding, H.; Chen, L.Q. The transmissibility of nonlinear energy sink based on nonlinear output frequency-response functions. *Commun. Nonlinear Sci. Numer. Simul.* **2017**, *44*, 184192. [CrossRef]
11. Gendelman, O.V.; Starosvetsky, Y. Quasi-periodic response regimes of linear oscillator coupled to nonlinear energy sink under periodic forcing. *J. Appl. Mech.* **2007**, *74*, 325331. [CrossRef]
12. Guo, H.; Yang, T.; Chen, Y.; Chen, L.Q. Singularity analysis on vibration reduction of a nonlinear energy sink system. *Mech. Syst. Signal Process.* **2022**, *173*, 109074. [CrossRef]
13. Li, S.B.; Ding, H. A cellular strategy for enhancing the adaptability of nonlinear energy sinks to strong excitation. *Int. J. Dyn. Control* **2024**, *12*, 16711678. [CrossRef]
14. Zhang, Y.; Kong, X.; Yue, C.; Guo, J. Characteristic analysis and design of nonlinear energy sink with cubic damping considering frequency detuning. *Nonlinear Dyn.* **2023**, *111*, 15817–15836. [CrossRef]
15. Wang, X.; Mao, X.Y.; Ding, H.; Lai, S.K.; Chen, L.Q. Multi-resonance inhibition of a two-degree-of-freedom piecewise system by one nonlinear energy sink. *Int. J. Dyn. Control* **2023**, *12*, 221092127. [CrossRef]
16. Gendelman, O.V. Targeted energy transfer in systems with non-polynomial nonlinearity. *J. Sound Vib.* **2008**, *315*, 732745. [CrossRef]
17. Saeed, A.S.; Al-Shudeifat, M.A.; Vakakis, A.F. Rotary-oscillatory nonlinear energy sink of robust performance. *Int. J.-Non-Linear Mech.* **2019**, *117*, 103249. [CrossRef]
18. Gatti, G.; Brennan, M.J.; Kovacic, I. On the interaction of the responses at the resonance frequencies of a nonlinear two-degrees-of-freedom system. *Phys. D Nonlinear Phenom.* **2010**, *239*, 591–599. [CrossRef]
19. Wu, Z.; Seguy, S.; Paredes, M. Qualitative analysis of the response regimes and triggering mechanism of bistable nonlinear energy sinks. *Nonlinear Dyn.* **2022**, *109*, 32352. [CrossRef]
20. Starosvetsky, Y.; Gendelman, O.V. Attractors of harmonically forced linear oscillator with attached nonlinear energy sink. II: Optimization of a nonlinear vibration absorber. *Nonlinear Dyn.* **2008**, *51*, 47–57. [CrossRef]
21. Starosvetsky, Y.; Gendelman, O.V. Vibration absorption in systems with a nonlinear energy sink: Nonlinear damping. *J. Sound Vib.* **2009**, *324*, 916939. [CrossRef]
22. Liu, Y.; Mojahed, A.; Bergman, L.A.; Vakakis, A.F. A new way to introduce geometrically nonlinear stiffness and damping with an application to vibration suppression. *Nonlinear Dyn.* **2019**, *96*, 1819–1845. [CrossRef]
23. Moslemi, A.; Khadem, S.E.; Khazaee, M.; Davarpanah, A. Nonlinear vibration and dynamic stability analysis of an axially moving beam with a nonlinear energy sink. *Nonlinear Dyn.* **2021**, *104*, 1955–1972. [CrossRef]
24. Zang, J.; Zhang, Y.W. Responses and bifurcations of a structure with a lever-type nonlinear energy sink. *Nonlinear Dyn.* **2019**, *98*, 889906. [CrossRef]
25. Li, H.B.; Ding, H.; Chang, T.C.; Chen, L.Q. Nonlinear dynamics of a track nonlinear energy sink. *Nonlinear Dyn.* **2024**, *112*, 11803–11827. [CrossRef]
26. Li, S.B.; Ding, H. Effective damping zone of nonlinear energy sinks. *Nonlinear Dyn.* **2023**, *111*, 18605–18629. [CrossRef]
27. Lu, Z.; Brennan, M.J.; Chen, L.Q. On the transmissibilities of nonlinear vibration isolation systems. *J. Sound Vib.* **2016**, *375*, 2837. [CrossRef]
28. Shen, Y.; Sui, P.; Wang, X. Performance analysis and optimization of bimodal nonlinear energy sinks. *Nonlinear Dyn.* **2023**, *111*, 16813–16830. [CrossRef]

29. Geng, X.F.; Ding, H.; Mao, X.Y.; Chen, L.Q. A ground-limited nonlinear energy sink. *Acta Mech. Sin.* **2022**, *38*, 521558. [CrossRef]
30. Moslemi, A.; Homaeinezhad, M.R. Effects of viscoelasticity on the stability and bifurcations of nonlinear energy sinks. *Appl. Math. Mech.* **2023**, *44*, 141158. [CrossRef]
31. Li, X.; Mojahed, A.; Chen, L.Q.; Bergman, L.A.; Vakakis, A.F. Shock response mitigation of a large-scale structure by modal energy redistribution facilitated by a strongly nonlinear absorber. *Acta Mech. Sin.* **2022**, *38*, 121464. [CrossRef]
32. Zhang, Z.; Ding, H.; Zhang, Y.W.; Chen, L.Q. Vibration suppression of an elastic beam with boundary inerter-enhanced nonlinear energy sinks. *Acta Mech. Sin.* **2021**, *37*, 387401. [CrossRef]
33. Gourc, E.; Michon, G.; Seguy, S.; Berlioz, A. Experimental investigation and design optimization of targeted energy transfer under periodic forcing. *J. Vib. Acoust.* **2014**, *136*, 021021. [CrossRef]
34. Chen, L.; Liao, X.; Xia, G.; Sun, B.; Zhou, Y. Variable-potential bistable nonlinear energy sink for enhanced vibration suppression and energy harvesting. *Int. J. Mech. Sci.* **2023**, *242*, 107997. [CrossRef]
35. Gomez, F.; Fermandois, G.A.; Smith, B.F.S., Jr. Optimal design of nonlinear energy sinks for mitigation of seismic response on structural systems. *Eng. Struct.* **2021**, *232*, 11175. [CrossRef]
36. Chen, Z.; Guo, B.; Cheng, C.; Shi, H.; Yang, Y. Chaotic dynamics-based analysis of broadband piezoelectric vibration energy harvesting enhanced by using nonlinearity. *Shock Vib.* **2016**, *11*, 10709622. [CrossRef]
37. Xiong, L.; Tang, L.; Liu, K.; Mace, B.R. Effect of electromechanical coupling on dynamic characteristics of a piezoelectric nonlinear energy sink system. *J. Vib. Eng. Technol.* **2021**, *9*, 687699. [CrossRef]
38. Liu, Z.; Wang, X.; Ding, S.; Zhang, R.; McNabb, L. A new concept of speed-amplified nonlinear electromagnetic vibration energy harvester through fixed pulley wheel mechanisms and magnetic springs. *Mech. Syst. Signal Process.* **2019**, *126*, 305325. [CrossRef]
39. Khairul, M.A.; Doroodchi, E.; Azizian, R.; Moghtaderi, B. Advanced applications of tunable ferrofluids in energy systems and energy harvesters: A critical review. *Energy Convers. Manag.* **2017**, *149*, 660674. [CrossRef]
40. Wu, S.; Luk, P.C.K.; Li, C.; Zhao, X.; Jiao, Z.; Shang, Y. An electromagnetic wearable 3-DoF resonance human body motion energy harvester using ferrofluid as a lubricant. *Appl. Energy* **2017**, *197*, 364374. [CrossRef]
41. Ouyang, X.; Cao, S.; Hou, Y.; Li, G.; Huang, X. Nonlinear dynamics of a dual-rotor system with active elastic support/dry friction dampers based on complex nonlinear modes. *Int. J. Non-Linear Mech.* **2024**, *166*, 104856. [CrossRef]
42. Wang, T.; Tang, Y.; Yang, T.; Ma, Z.S.; Ding, Q. Bistable enhanced passive absorber based on integration of nonlinear energy sink with acoustic black hole beam. *J. Sound Vib.* **2023**, *544*, 117409. [CrossRef]
43. Tao, K.; Tang, L.; Wu, J.; Lye, S.W.; Chang, H.L. Investigation of multimodal electret-based MEMS energy harvester with impact-induced nonlinearity. *J. Microelectromech. Syst.* **2018**, *27*, 276288.
44. Phan, H.; Shin, D.M.; Jeon, S.H. Aerodynamic and aeroelastic flutters driven triboelectric nanogenerators for harvesting broadband airflow energy. *Nano Energy* **2017**, *33*, 476–484. [CrossRef]
45. Ravichandran, A.N.; Calmes, C.; Serres, J.R.; Ramuza, M.; Blayac, S. Compact and high-performance wind-actuated venturi triboelectric energy harvester. *Nano Energy* **2019**, *62*, 449–457. [CrossRef]
46. Lu, Z.Q.; Zhao, L.; Fu, H.L. Ocean wave energy harvesting with high energy density and self-powered monitoring system. *Nat. Commun.* **2024**, *15*, 6513. [CrossRef] [PubMed]
47. Zhao, L.C.; Zou, H.X.; Wei, K.X.; Zhou, S.X.; Meng, G.; Zhang, W.M. Mechanical intelligent energy harvesting: From methodology to applications. *Adv. Energy Mater.* **2023**, *29*, 16146832. [CrossRef]
48. Kremer, D.; Liu, K. A nonlinear energy sink with an energy harvester: Harmonically forced responses. *J. Sound Vib.* **2017**, *410*, 287–302. [CrossRef]
49. Remick, K.; Quinn, D.D.; McFarland, D.M.; Bergman, L.; Vakakis, A.F. High-frequency vibration energy harvesting from repeated impulsive forcing utilizing intentional dynamic instability caused by strong nonlinearity. *J. Intell. Mater. Syst. Struct.* **2017**, *28*, 468–487. [CrossRef]
50. Remick, K.; Quinn, D.D.; McFarland, D.M.; Bergman, L.; Vakakis, A.F. High-frequency vibration energy harvesting from impulsive excitation utilizing intentional dynamic instability caused by strong nonlinearity. *J. Sound Vib.* **2016**, *370*, 259–279. [CrossRef]
51. Zhou, S.; Li, Z.; Zhou, S. A two-degree-of-freedom nonlinear electromagnetic energy harvester in rotational motion. *Mech. Syst. Signal Process.* **2024**, *220*, 111695.
52. Xu, C.; Liang, Z.; Ren, B.; Di, W.; Luo, H.; Dong, W.; Wang, K.; Chen, Z. Bistable energy harvesting based on a simply supported piezoelectric buckled beam. *J. Appl. Phys.* **2013**, *114*, 114507. [CrossRef]
53. Bai, S.; Cui, J.; Zheng, Y.; Li, G.; Liu, T.; Liu, Y.; Hao, C.C.; Xue, C.Y. Electromagnetic–triboelectric energy harvester based on vibration-to-rotation conversion for human motion energy exploitation. *Appl. Energy* **2023**, *329*, 120292.
54. Mace, B.R. On the use of piezoelectric nonlinear energy sinks for vibration isolation and energy harvesting. *ASME J. Vib. Acoust.* **2018**, *7*, 20187968.
55. Tian, W.; Li, Y.; Yang, Z.; Li, P.; Zhao, T. Suppression of nonlinear aeroelastic responses for a cantilevered trapezoidal wing. *Int. J. Mech. Sci.* **2020**, *172*, 105417.

56. Nie, X.; Yang, M.; Lin, X.; Lin, T.; Yan, Z.; Wang, L. Vibration suppression and energy harvesting of a two-degree-of-freedom main structure coupled with a bistable nonlinear energy sink under transient excitation. *J. Vib. Eng. Technol.* **2024**, *12*, 2301–2323.
57. Liu, X.C.; Ding, H.; Geng, X.F.; Wei, K.X.; Lai, S.K.; Chen, L.Q. A magnetic nonlinear energy sink with quasi-zero stiffness characteristics. *Nonlinear Dyn.* **2024**, *112*, 5895–5918. [CrossRef]
58. Zeng, Y.; Ding, H.; Li, Y.; Chen, L. A tristable nonlinear energy sink to suppress strong excitation vibration. *Mech. Syst. Signal Process.* **2023**, *203*, 110768.
59. Dekemele, K.; Van Neck, J.; De Gersem, H. Tailored nonlinear stiffness and geometric damping: Applied to a bistable vibration absorber. *Int. J. Mech. Sci.* **2023**, *248*, 108198.
60. Menck, P.J.; Heitzig, J.; Marwan, N.; Kurths, J. How basin stability complements the linear-stability paradigm. *Nat. Phys.* **2013**, *9*, 89. [CrossRef]

Disclaimer/Publisher's Note: The statements, opinions and data contained in all publications are solely those of the individual author(s) and contributor(s) and not of MDPI and/or the editor(s). MDPI and/or the editor(s) disclaim responsibility for any injury to people or property resulting from any ideas, methods, instructions or products referred to in the content.